APPLIED SCIENCES AND ENGINEERING

Machine reading and recovery of colors for hemoglobin-related bioassays and bioimaging

Sang Mok Park[1], Semin Kwon[1], Yuhyun Ji[1], Haripriya Sakthivel[1], Jung Woo Leem[1], Yunsang Kwak[2], Jonathan Huang[1,3], George T.-C. Chiu[4], Andrew R. O'Brien[3,5], Raymond L. Konger[5,6,7,8], Ying Wang[3,9], Young L. Kim[1,8,10,11]*

Despite advances in machine learning and computer vision for biomedical imaging, machine reading and learning of colors remain underexplored. Color consistency in computer vision, color constancy in human perception, and color accuracy in biomedical imaging are intertwined, complicating digital color–based diagnostics. Existing color reference charts and correction algorithms are inadequate for mobile health (mHealth) and telemedicine in digital health applications where detecting subtle color changes is critical. We present a machine reading and learning platform for color recognition and quantification to extract diagnostic information from colors. A unique combination of spectroscopic gamut determination, reference color optimization, nonsubjective quantification metrics, and neural network–based color recovery retrieves absolute colors of biological tissue. Studies on inflammation bioimaging of photocarcinogenesis and mHealth blood hemoglobin assessment demonstrate accuracy and precision in color recovery across diverse acquisition scenarios. The reported framework overcomes limitations of conventional colorimetric detection, enabling machine-compatible color-based bioassays and bioimaging, advancing digital diagnostics.

INTRODUCTION

Recent advances in machine learning for computer vision in biomedical imaging have focused on spatial analyses and feature extraction (*1*–*3*), often disregarding the valuable information conveyed by intrinsic colors. As a result, there remains a critical need for machine learning of colors in biomedical imaging. Color recognition and quantification in biomedical imaging including photography are complex, involving both acquisition and display (*4*, *5*). As an emerging bioimaging modality, smartphone imaging using onboard cameras is becoming increasingly important in mobile health (mHealth) and telemedicine applications where accurate and precise color detection plays a crucial role (*6*–*9*). "Color consistency" in computer vision, "color constancy" in human perception, and "color accuracy" in biomedical imaging are distinct yet interrelated aspects of color science. Specifically, color consistency is crucial for color correction and reproduction in computer vision (*10*). Color constancy is a well-established field in human color perception that primarily aims to achieve identical perceptual responses (*11*–*13*). Color accuracy in biomedical imaging encompasses both the detection and reproduction of exact colors with the potential for accurate and precise digital diagnostics (*4*, *5*).

To achieve machine-favorable color recognition and quantification, it is essential to overcome the limitations associated with conventional colorimetric detection, which are inherently rooted in human color perception (*14*). Machine readability of colors of a sample in a photo is influenced by multiple factors, including devices (e.g., sensors and optics), light conditions (e.g., natural or artificial lighting), image file formats, color balance algorithms (e.g., white balancing), and color correction methods. These complexities result in substantial color variations in photos despite using an identical sample. Metamerism can also occur when two samples with different spectral profiles yield identical digital color values under specific light conditions. For machine-readable color quantification and recognition, the absolute colors of the sample must be standardized and recovered without being affected by physical acquisition conditions. Bias introduced by human vision and color perception also needs to be factored out to enable automated diagnostics and minimize reliance on healthcare professionals.

For color correction, calibration, or reproduction, several color standards or reference charts (e.g., Macbeth ColorChecker, X-Rite ColorChecker, Pantone Color Match Card, Spyder Checkr Photo, IFRAO, and IT8) have been developed (*15*). Historically, Chevreul Cercle Chromatique, published in 1861, is one of the oldest known color charts (*16*), and Macbeth ColorChecker is currently the most commonly used (*15*, *17*). Dating back to the Late Middle Ages (1300 to 1500), urine wheels and uroscopy charts represent the earliest examples of diagnostic color reference charts (*18*, *19*). Conventional color charts or a few customized colors are frequently used to improve colorimetric diagnostics (*20*–*28*) (table S1), including cancer (*29*–*32*), wounds (*33*–*35*), diabetes (*36*, *37*), erythema (*38*), skin injuries (*39*), autoimmune diseases (*40*), and jaundice (*41*, *42*). Bioassay-relevant reference colors can enhance paper-based immunoassays such as pH strips (*43*, *44*), urinalysis (*45*), peroxide strips (*46*), and hemoglobin (Hgb) strips (*47*). Even simple conventional color charts can benefit remote patient monitoring and telemedicine settings (*27*, *48*, *49*).

[1]Weldon School of Biomedical Engineering, Purdue University, West Lafayette, IN 47907, USA. [2]Department of Mechanical System Engineering, Kumoh National Institute of Technology, 61 Daehak-ro, Gumi-si, Gyeongsangbuk-do 39177, Republic of Korea. [3]Department of Medicine, Indiana University School of Medicine, Indianapolis, IN 46202, USA. [4]School of Mechanical Engineering, Purdue University, West Lafayette, IN 47907, USA. [5]Indiana University Simon Cancer Center, Indianapolis, IN 46202, USA. [6]Department of Pathology and Laboratory Medicine, Indiana University School of Medicine, Indianapolis, IN 46202, USA. [7]Department of Dermatology, Indiana University School of Medicine, Indianapolis, IN 46202, USA. [8]Richard L. Roudebush Veterans' Administration Medical Center, Indianapolis, IN 46202, USA. [9]Department of Anesthesia, Stark Neurosciences Research Institute, Indiana University School of Medicine, Indianapolis, IN 46202, USA. [10]Purdue Institute for Cancer Research, West Lafayette, IN 47907, USA. [11]Purdue Quantum Science and Engineering Institute, West Lafayette, IN 47907, USA.
*Corresponding author. Email: youngkim@purdue.edu

However, the existing color correction methods are inadequate for machine-readable and nonsubjective diagnostic purposes. First, it is theoretically impossible to achieve accurate and precise color detection across all diverse colors using a single universal color gamut (*25*, *50*–*52*). Although an application-specific color gamut tailored to diagnostic needs is essential, identifying relevant yet subtle color derivatives can be challenging, requiring extensive spectroscopic measurements and analyses. Second, undersampling the reference colors in conventional color charts fundamentally compromises the fidelity of color correction (*53*–*57*). Color correction and calibration computations with a limited number of reference colors are susceptible to random and systematic errors (e.g., Gaussian, impulse, photon, and speckle noise) in various photo acquisitions (*58*–*61*). Machine learning approaches leveraging more reference colors can outperform conventional color correction methods (*58*, *61*). Third, typical regression-based color corrections (also known as lookup table and interpolation) (*62*) in computer vision require manual and scene/sample-specific fine-tuning, making automated color quantification challenging (*53*, *56*, *60*, *63*).

We introduce machine reading and learning platforms for color recognition and quantification, aimed at color-based diagnostic applications in bioassays and bioimaging to address the inherent limitations of conventional color corrections. Our work consists of four main components: designing color reference charts, selecting quantification metrics (both perception-based and objective measures), developing neural network–based color recovery algorithms, and validating our methods through experimental studies. First, a color gamut determined through spectroscopic analyses allows the design of reference colors optimized for machine readability of biological tissue. Second, the color space, illuminant, and quantification metrics are tailored for color-based diagnostic bioimaging and bioassay applications. Third, machine learning algorithms (statistical regression and neural networks) for digital color recovery enable fully automated and high-fidelity color quantification across diverse photo acquisition settings. Last, the proposed platform is demonstrated through extensive comparisons with conventional color corrections, including experimental animal imaging of skin cancer–related inflammation and noninvasive mHealth assessments of blood Hgb levels from peripheral tissue. As the recovered color values serve as frontend inputs to application-specific models, the experimental evaluations focus on comparing model performance among different color corrections.

RESULTS

Diverse photo acquisitions related to devices, light conditions, and file formats

Diverse photo acquisition scenarios present an inherent challenge for accurate and precise color reading and learning in color-based diagnostic bioassays and bioimaging (see note S1 and Fig. 1). From an illumination standpoint, different types of white light sources have distinct spectral profiles despite their grossly white-appearing features (Fig. 1, A and B, and fig. S1). Such diverse spectral characteristics of light sources fundamentally limit white balancing (also known as computational color constancy), making it challenging to achieve exposure invariance (Fig. 1C and movie S1) (*64*). From a device standpoint, a digital trichromatic camera (three-color image sensor) has unique red-green-blue (RGB) spectral response functions (also known as spectral sensitivity) as a function of the wavelength of light λ (Fig. 1D). Notably, the RGB spectral responses of smartphone cameras exhibit model-specific variations (fig. S2) (*65*–*68*), resulting in device-dependent RGB color values (Fig. 1E). From a file format standpoint, the degree of color compression is substantially influenced by the image file format (Fig. 1F) (*64*). JPEG, the most common 8-bit depth format, uses lossy compression to reduce the file size, whereas RAW (10-bit depth, also known as DNG) minimizes data compression and rendering. Recent high-end smartphones provide Pro Mode or ProRAW for 10-bit depth in each RGB channel. In telemedicine settings (Fig. 1F), two-way video conferencing between a health care provider and a patient introduces additional file formats (e.g., MP4). When photos of the same sample are captured under various photo acquisition scenarios (Fig. 1G), recovered color values must converge to the ground truth values, provided that color recovery is performed accurately and precisely.

Color gamut of conventional color reference and calibration charts

Because of the absence of universal color canonicalization at the device level, conventional color corrections rely on physical color standards or reference charts. Specifically, a color chart is used to establish a mapping between the measured and ground truth color values by analyzing how the chart's colors appear in the captured photo. This mapping is then applied to adjust the color values in the area of interest or across the entire photo. The fundamental limitation of the conventional color charts is their overly general and nonspecific color gamuts; a broad range of reference colors is selected for general photography (*25*, *50*, *51*, *69*). As the most commonly used color chart, Macbeth ColorChecker (or X-Rite ColorChecker) consists of reference colors that cover the sRGB color space, one of the largest color gamuts (Fig. 2A) (*15*, *17*). Figure 2 (B to D) shows the broad range of International Commission on Illumination (CIE) XYZ values of the reference colors in Macbeth ColorChecker, measured using a scientific laboratory spectrometer (see note S1 and fig. S3). Using a diffuse (Lambertian) reflectance standard with 99% reflectivity across the entire visible range, spectral normalization is equivalent to using CIE standard illuminant E (equal energy radiator), resulting in a flat spectral profile of illumination (see Materials and Methods). In addition, the CIE L* values (lightness) of the reference colors are within the broad range of 10 to 100 in the CIE LAB color space (Fig. 2D).

Definition of blood Hgb gamut from physiologically possible spectra

We identify a physiologically relevant color gamut of biological tissue for peripheral perfusion and blood Hgb. Hgb is one of the most dominant chromophores in biological tissue including the skin (*70*, *71*). It is a vital protein in red blood cells responsible for oxygen transport and is associated with various medical conditions, diseases, and disorders beyond hematology. A spectral database augmented by parametric spectral modeling (see Materials and Methods) allows us to define the gamut relevant to blood Hgb and peripheral perfusion, accounting for light scattering (Rayleigh and Mie) and absorption in biological tissue (Table 1). A physiologically plausible range of blood Hgb–related color variations is determined by using 10,000 spectral data from whole blood and 12,240 spectral data from peripheral tissue (see Materials and Methods, note S1, and Fig. 2, E to I). Figure 2G reveals a unique triangular gamut defined by three primary points of CIE xy chromaticity: $(x, y) = (0.30, 0.31), (0.47, 0.42),$

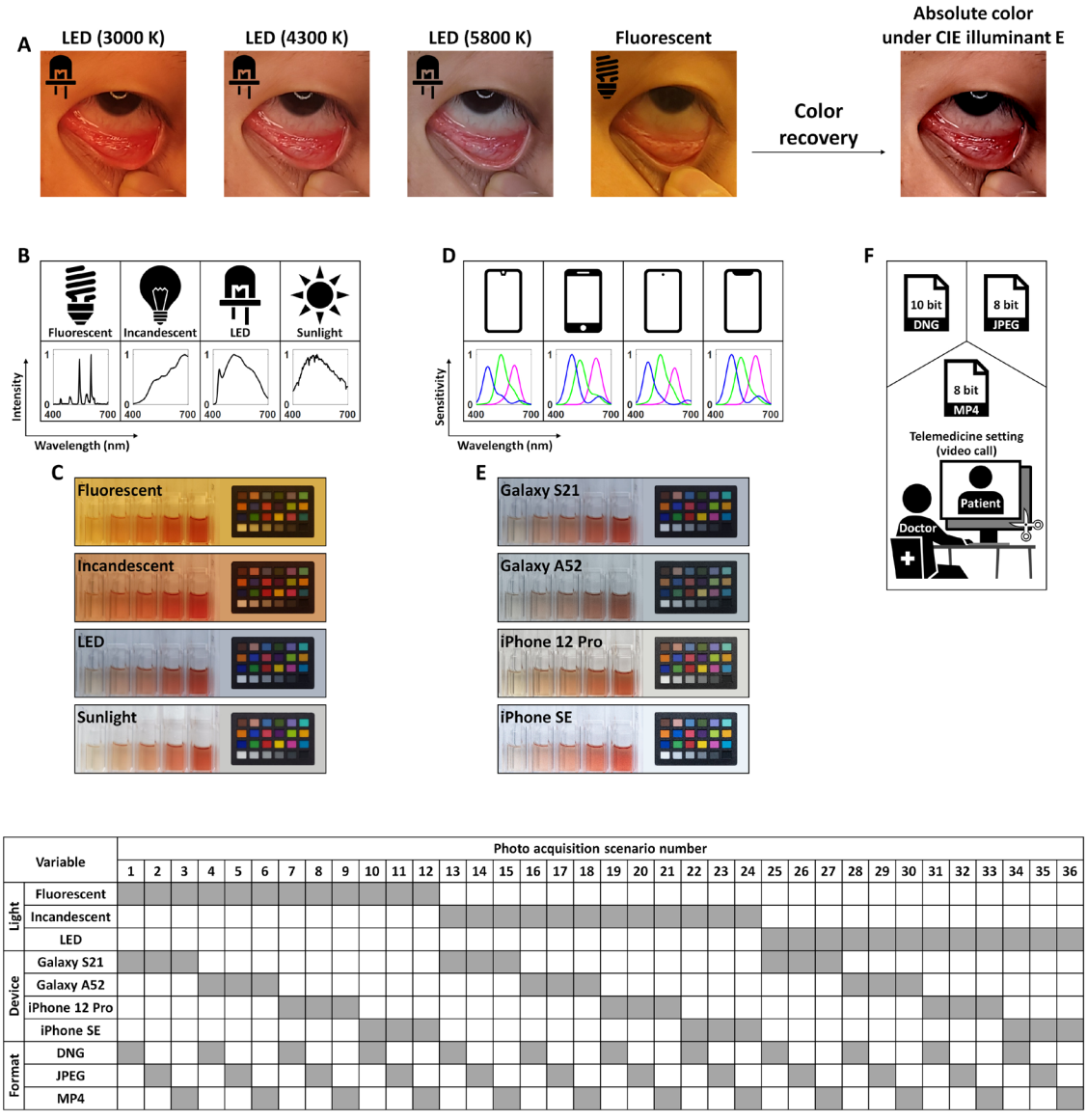

Fig. 1. Challenges in computer color vision for color-based diagnostic bioassays and bioimaging. (**A**) Detrimental color variations in digital photos of biological tissue captured under various white-light illumination conditions: light-emitting diodes (LEDs) with color temperature of 3000, 4300, and 5800 K, as well as fluorescent tube light. The colors under CIE illuminant E (equal energy radiator or spectrally uniform illumination) can be considered absolute. CIE illuminant E is achieved through spectral normalization using a diffuse (Lambertian) reflectance standard (see Materials and Methods). (**B**) Light conditions having distinct spectral profiles: fluorescent tube, incandescent light, white LED, and sunlight (fig. S1). (**C**) Representative photos of whole blood–mimicking samples in cuvettes at different hemoglobin (Hgb) concentrations, acquired under various light conditions. A conventional color chart (Macbeth ColorChecker or X-Rite ColorChecker) is juxtaposed with the samples. (**D**) Smartphone model–dependent RGB spectral response functions (also known as spectral sensitivity): Apple iPhone 12 Pro, Apple iPhone SE, Samsung Galaxy S21, and Samsung Galaxy A52 (fig. S2). (**E**) Representative photos captured using various smartphone models. (**F**) File formats with different bit depths (color depths) in the R, G, and B color channels: JPEG (8-bit depth), RAW (10-bit depth), and MP4 (8-bit depth). (**G**) Representative photo acquisition scenarios based on combinations of light conditions (B), smartphone models (D), and file formats (F). When multiple photos of the same sample are captured under varying conditions, accurate and precise color recovery ensures that recovered color values converge to the ground truth.

and (0.63, 0.33). This gamut has CIE L* values (lightness) within a range of 40 to 90 (Fig. 2I). The Hgb gamut is much narrower than the sRGB color gamut corresponding to Macbeth ColorChecker (Fig. 2G). The Hgb gamut encompasses a gamut that captures the largest library of human skin colors and tones (i.e., Pantone SkinTone Guide), influenced by melanin content (fig. S4). Note that Pantone SkinTone Guide includes the widely recognized skin tone scales: Fitzpatrick Scale and Monk Skin Tone Scale (*72*).

Selection of color space, illuminant, and quantification metric

Unlike conventional colorimetric diagnostics, the machine readability of colors should not be influenced by human color perception or variations in photo acquisition conditions. First, the use of CIE illuminant E allows us to define the absolute colors of a sample of interest. While CIE illuminant E is regarded as a theoretical reference, spectral normalization involving a reflectance standard can be

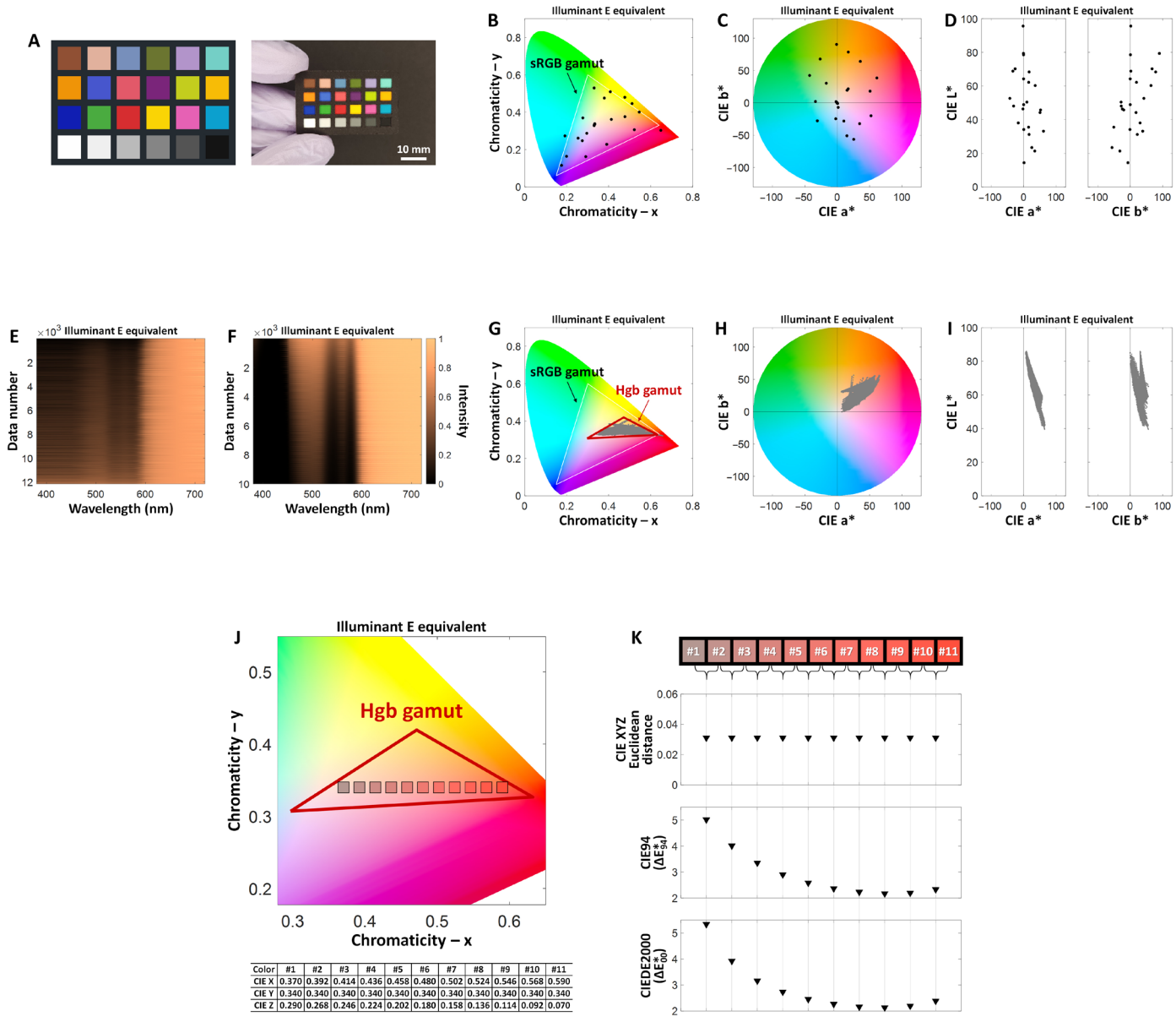

Color	#1	#2	#3	#4	#5	#6	#7	#8	#9	#10	#11
CIE X	0.370	0.392	0.414	0.436	0.458	0.480	0.502	0.524	0.546	0.568	0.590
CIE Y	0.340	0.340	0.340	0.340	0.340	0.340	0.340	0.340	0.340	0.340	0.340
CIE Z	0.290	0.268	0.246	0.224	0.202	0.180	0.158	0.136	0.114	0.092	0.070

Fig. 2. Color gamut of blood Hgb and peripheral tissue perfusion and color quantification metrics for machine readability and learning. (**A**) Macbeth ColorChecker containing 24 reference colors used for general photography. (**B**) Corresponding CIE xy chromaticity values under CIE illuminant E, measured using a spectrometer and a reflectance standard. The wide gamut of Macbeth ColorChecker overlaps with the sRGB color space. (**C**) Corresponding CIE LAB values under CIE illuminant E on the *a** and *b** axes. (**D**) Corresponding L* values as functions of a* and b* values. (**E** and **F**) Parametric spectral modeling of biological tissue (peripheral tissue and blood samples). Physiologically possible color variations are captured by 12,240 synthesized spectral data of peripheral tissue (E) and 10,000 synthesized spectral data of whole blood (F) (see Materials and Methods). (**G**) Blood Hgb gamut defined by three primary points of CIE xy chromaticity: $(x, y) = (0.30, 0.31)$, $(0.47, 0.42)$, and $(0.63, 0.33)$. (**H**) Corresponding CIE LAB values on the *a** and *b** axes. (**I**) Corresponding L* values as functions of a* and b* values. (**J** and **K**) Importance of CIE XYZ Euclidean distance metric for machine readability and learning in color-based diagnostics, compared to Delta E values including CIE94 (ΔE^*_{94}) and CIEDE2000 (ΔE^*_{00}). Eleven representative colors are selected from the Hgb gamut, with equal CIE XYZ Euclidean distances between all pairs of adjacent colors. Delta E values incorporate human visual judgment and perception.

used to factor out the spectral response of the illumination and system, which is equivalent to using CIE illuminant E (see Materials and Methods). Second, the CIE XYZ color space is machine-preferred for describing the direct relationship between reflectance spectra and the three color responses (color matching functions) (*73*–*75*). Although the L* component in the CIE LAB color space is beneficial for matching the human perception of lightness, this color space includes normalization terms for a white reference illuminant and uses nonlinear relationships for L*, a*, and b*. Third, the CIE XYZ Euclidean distance allows for the nonsubjective, machine-preferred quantification of color differences (or distances) between two adjacent colors. Although Delta E serves as the conventional metric for

Table 1. Physiologically relevant ranges of model parameters in spectral modeling of peripheral tissue perfusion and blood Hgb samples for tissue colors.

Parameter	Parameter description	Relevant range
a_1	Scattering slope	−0.5–2
a_2	Optical path length · blood volume fraction	0.02–0.1 (mm)
a_3	Effective blood vessel diameter	18–70 (μm)
a_4	Blood Hgb level	4–20 (g dl^{-1})
a_5	Blood oxygen saturation	50–100 (%)

color differences, it reflects human visual judgment and color perception (*76*–*79*), which introduce unintended weighting effects that hinder machine readability.

Figure 2 (J and K) supports the selection of color space, distance, and illuminant for calculating color differences between two adjacent colors within the Hgb gamut. Eleven Hgb-related colors are generated for evaluation with evenly spaced CIE XYZ and CIE xy chromaticity values within the Hgb gamut (Fig. 2J). The color differences between all pairs of adjacent colors are then calculated by three distinct color metrics: CIE XYZ Euclidean distance, CIE94 (ΔE^*_{94}), and CIEDE2000 (ΔE^*_{00}). Although the combined use of the three metrics provides more comprehensive and reliable quantification, the Delta E values (CIE94 and CIEDE2000) clearly introduce nonlinearities due to perceptual uniformity despite the same CIE XYZ Euclidean distance (Fig. 2K). The CIE XYZ Euclidean distance under CIE illuminant E is the most suitable metric for quantifying color differences compared to reference colors in color-based diagnostic bioimaging and bioassay applications. In other words, colorimetric diagnostics based on human perception are fundamentally not applicable to machine-readable color-based diagnostics.

Design of Hgb gamut–based color charts and neural network–based color recovery

On the basis of the defined Hgb gamut (Fig. 2, G to I), we design a color chart (hereafter referred to as HemaChrome) for color recovery of blood Hgb and peripheral perfusion (Fig. 3, A to E). HemaChrome includes 116 reference colors: 100 Hgb-related colors, 12 primary colors, and four grayscale colors (Fig. 3, B to E, and figs. S5 and S6). The primary colors, along with grayscale colors (fig. S6, A to C), are included to stably interpolate color outliers outside the Hgb gamut and compute the spectral response functions of the smartphone camera (*65*–*68*). All Hgb-related reference colors in HemaChrome are selected within the Hgb gamut with CIE xy chromaticity and CIE L* values (lightness) uniformly distributed inside it (fig. S7, A to C). The CIE XYZ values of 116 reference colors in HemaChrome are converted to sRGB to ensure accurate color representation, resulting in the final chart design in Adobe InDesign (Fig. 3B). To ensure the accessibility, practicality, and scalability, HemaChrome charts are printed using a commercially available inkjet printer (imagePROGRAF PRO-1000, Canon) with manufacturer-recommended printing calibration (see Materials and Methods). The printing reproducibility and color fade resistance (minimum shelf-life with sunlight exposure) of HemaChrome further support its practicality and scalability (see note S2).

On the basis of HemaChrome, we develop a neural network algorithm for fully automated and high-fidelity color recovery under diverse acquisition scenarios (see Materials and Methods). The neural network is designed to overcome the intrinsic limitation of conventional regression-based color corrections (also known as lookup table and interpolation). The primary drawback of regression-based color corrections using Macbeth ColorChecker (see Materials and Methods) is their lack of generalizability. Beyond linear color correction (Eq. 9), a unique set of higher-degree RGB polynomial (or root-polynomial) expansion terms in Eq. 10 is frequently incorporated (*56*, *63*) but is highly scene- and sample-specific, depending on various photo acquisition conditions (*53*, *56*, *60*, *62*, *63*). Consequently, an appropriate set of polynomial expansions (Eq. 10) must be selected manually and empirically for each photo acquisition.

Figure 3A illustrates the concept of color recovery using a neural network with HemaChrome. The neural network is not pretrained on any existing dataset. It is specifically trained for each photo, where the HemaChrome chart is juxtaposed with the sample of interest. The training dataset consists of the color values of the reference colors in HemaChrome. The input is the acquired RGB values of these reference colors in the given photo, while the output is the corresponding CIE XYZ values measured by a spectrometer under CIE illuminant E. Once the neural network is trained for a particular photo, the RGB values acquired from the sample of interest in the photo are input into the trained network, which then outputs the corresponding CIE XYZ values. In this respect, the neural network–based color recovery algorithm is referred to as "one-shot transduction" learning (as opposed to inductive learning) because the training is scene- and sample-specific (*80*).

The 116 reference colors in HemaChrome represent an optimal selection based on physical size constraints and neural network requirements (see note S3, fig. S8, and eqs. S1 to S4), serving as the training dataset for the neural network–based color recovery algorithm. Because of the relatively small amount of training data, the network is concise with three layers: an input layer, a hidden layer, and an output layer. Sigmoid activation functions are used as they are highly suitable for shallow networks, supported by the universal approximation theory (*81*, *82*). The hidden layer mimics a wide range of possible terms of RGB polynomial (root-polynomial) expansions in Eq. 10, eliminating the need for manual selection of appropriate expansion terms. Thus, this color recovery algorithm design is analogous to physics-informed deep learning or physics-driven machine learning (*83*–*85*).

Figure 3 (F to J) shows Macbeth ColorChecker and HemaChrome (116 reference colors) with regression-based color correction and HemaChrome with neural network–based color recovery. The eight Hgb scale patches in Tallquist Haemoglobin Scale (equivalent to World Health Organization Haemoglobin Colour Scale) are used as

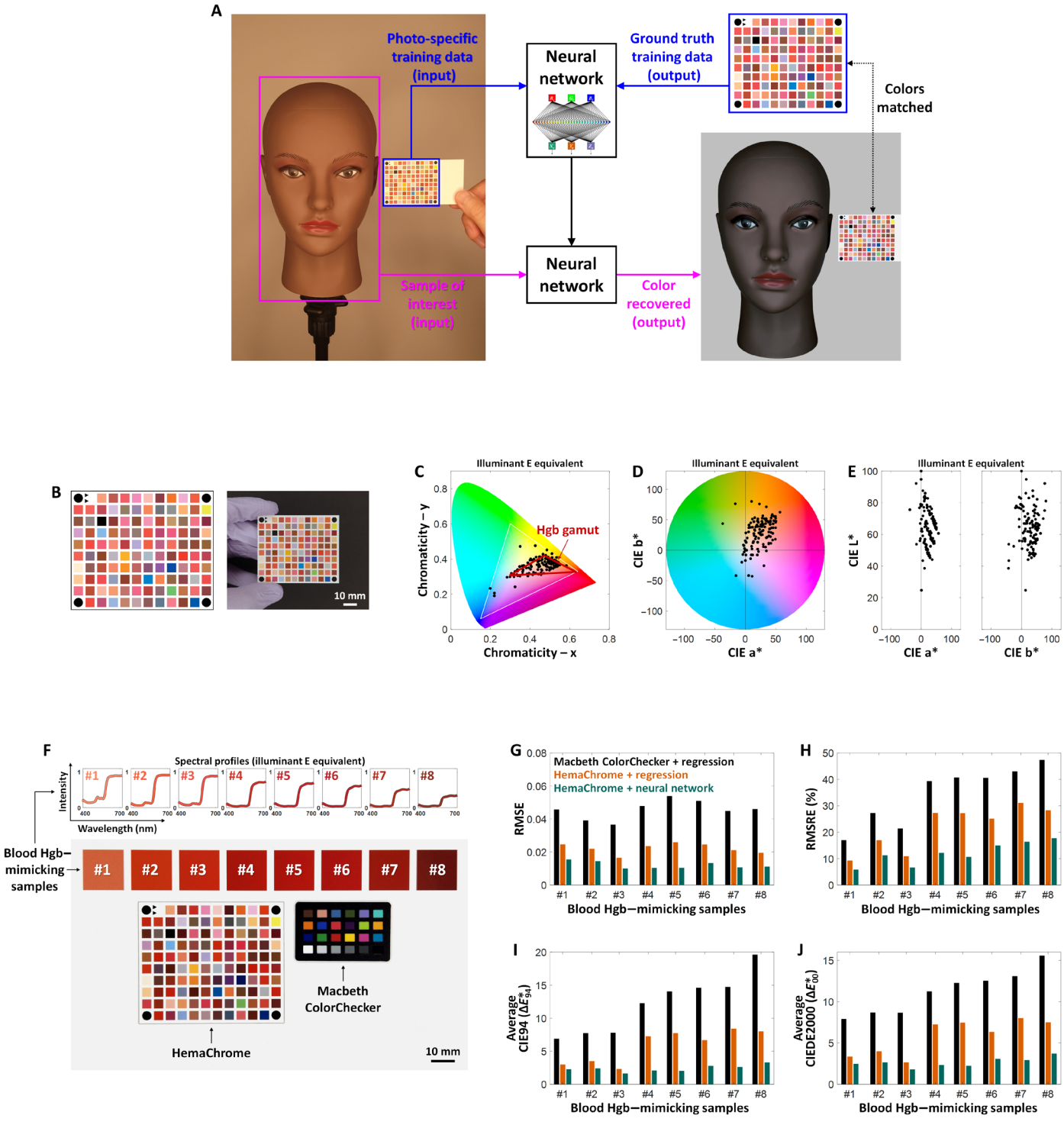

Fig. 3. Importance of color gamuts and computational algorithms on color correction performance. (**A**) One-shot transduction learning of neural network–based color recovery with HemaChrome. The neural network is trained for each photo without relying on any preexisting training dataset. The training dataset consists of the color values of the reference colors in HemaChrome. Once trained on the specific photo, the network processes the RGB values acquired from the sample of interest in the photo to recover the corresponding CIE XYZ values. (**B**) HemaChrome chart with 116 reference colors for neural network–based color recovery. (**C**) Corresponding CIE xy chromaticity values under CIE illuminant E, measured using a spectrometer and a reflectance standard. (**D**) Corresponding CIE LAB values under CIE illuminant E on the *a** and *b** axes. (**E**) Corresponding L* values as functions of a* and b* values. (**F**) Representative photo of blood Hgb–mimicking samples to recover their absolute colors (under CIE illuminant E). (**G** to **J**) Average color differences between the ground truth and recovered CIE XYZ values for each test sample from photos captured across 36 diverse photo acquisition scenarios (Fig. 1G). The root mean square error (RMSE) (G), root mean square relative error (RMSRE) (H), average CIE94 (ΔE^*_{94}) (I), and average CIEDE2000 (ΔE^*_{00}) (J) are compared (eqs. S1, S2, S6, and S7). Among the three color correction methods, neural network color recovery using HemaChrome consistently returns minimal errors across all test samples.

blood Hgb mimicking test samples. The ground truth CIE XYZ values under CIE illuminant E of these patches are calculated from spectral measurements (Fig. 3F). We analyze photos of the same samples acquired under 36 photo acquisition scenarios (Fig. 1G and fig. S9) and recover the absolute colors of the test samples. The CIE XYZ Euclidean distances (eq. S5) between the ground truth and recovered CIE XYZ values are calculated for each sample under diverse acquisition scenarios. Regression-based color corrections show high fluctuations in CIE XYZ Euclidean distance, depending on the type of polynomial expansions (figs. S10 and S11). For simplicity, linear color correction (Eq. 9) is used to ensure fair comparisons between Macbeth ColorChecker and HemaChrome. Figure 3 (G to J) shows the average color differences (table S2), calculated using four distinct metrics (eqs. S1, S2, S6, and S7): the root mean square error (RMSE), root mean square relative error (RMSRE), average CIE94 (ΔE^*_{94}), and average CIEDE2000 (ΔE^*_{00}). HemaChrome using the neural network algorithm consistently returns the lowest color differences across all four metrics (Fig. 3, G to J, and fig. S12), outperforming the regression-based color corrections. In addition, the reported color recovery is relatively unaffected by smartphone camera imperfections (e.g., out-of-focusing, lens contamination, and vignetting) (fig. S13) due to the analyses in the color domain rather than the spatial domain.

Machine readability using self-test samples in Tallquist Haemoglobin Scale

We evaluate the machine color readability and quantification using the reference Hgb scale patches in Tallquist Haemoglobin Scale (*47*, *86*–*88*). The original intended use of Tallquist Haemoglobin Scale involves juxtaposing a drop of blood smeared onto filter paper for diagnosing anemia. However, it has inherent limitations; the color of the capillary blood sample on the filter paper is influenced by the blood sample volume, the filter paper properties, and the subjective nature of color comparisons (*87*). In our study, Tallquist Haemoglobin Scale serves as an excellent test sample due to its numerical Hgb values. The scale consists of eight Hgb patches ranging from lighter to darker shades, corresponding to blood Hgb levels of 4.7, 6.3, 7.8, 9.4, 10.9, 12.5, 14.1, and 15.6 g dl^{-1} (Fig. 4, A to D). For direct numerical machine readings of Hgb values, a blood Hgb level is modeled as a univariate polynomial function of the CIE X, Y, and Z values under CIE illuminant E: $\gamma_0 + \gamma_1 X + \gamma_2 Y + \gamma_3 Z + \cdots + \gamma_{3n} Z^n$, where γ_0 to γ_{3n} are the coefficients and the polynomial order n is up to six (see note S4). In other words, the recovered CIE XYZ values of the eight Hgb scale patches under specific photo acquisition conditions serve as the frontend input to return blood Hgb levels. The machine readability of the eight Hgb scale patches is then compared between neural network color recovery (HemaChrome) and adaptive regression color correction (Macbeth ColorChecker equivalent; fig. S6, A to C). Adaptive regression color correction involves selecting a specific set of polynomial expansions that returns the smallest error among the five types of expansion terms (Eq. 10) for a particular sample under a specific acquisition scenario (see note S3).

We calculate the color differences between the Hgb scale patch of 9.4 g dl^{-1} (used as a representative self-test sample) and other Hgb scale patches (Fig. 4, E and F), following color corrections with HemaChrome and Macbeth ColorChecker. HemaChrome consistently identifies the correct and closest Hgb scale patch (Fig. 4E), whereas Macbeth ColorChecker fails to detect subtle color differences (Fig. 4F). In Fig. 4G, the blood Hgb levels computed using HemaChrome closely match the actual Hgb values of the eight Hgb scale patches, as recovered from photos captured across diverse photo acquisition scenarios (Fig. 1G). This consistency is further demonstrated by minimal standard deviations (SDs) (table S3). In contrast, the blood Hgb levels computed using Macbeth ColorChecker show notable variations (Fig. 4H and table S4) despite adaptive regression color correction selecting the optimal set of polynomial expansion terms in Eq. 10 to minimize error. Notably, HemaChrome exhibits lower coefficients of variation than Macbeth ColorChecker across all Hgb scale patches (Fig. 4I and eqs. S8 and S9). This result highlights the critical role of the Hgb gamut in improving the accuracy and precision of blood Hgb–related color recovery because the absolute color values of the eight Hgb scale patches fall within the Hgb gamut used by HemaChrome (Fig. 4B).

Inflammation bioimaging of experimental cutaneous photocarcinogenesis

We examine the machine color readability and learning for bioimaging of inflammatory skin lesions associated with nonmelanoma skin cancer. As key components of the tissue microenvironment, chronic inflammatory hyperemia and angiogenesis substantially contribute to cutaneous photocarcinogenesis and skin cancer (*89*–*93*). Hyperspectral (or multispectral) imaging modalities are extensively used to detect such inflammatory changes by quantifying Hgb content and hemodynamics (*94*–*97*). However, conventional hyperspectral imaging systems face inherent limitations, including bulky equipment, slow data acquisition, low signal-to-noise ratio, and susceptibility to motion artifacts (*94*–*97*). As an alternative for bioimaging, HemaChrome with neural network color recovery can serve as the frontend input to reliably image inflammation foci and quantify Hgb content from a photo captured by a smartphone camera.

To investigate inflammatory hyperemia on animal skin in an experimental photocarcinogenesis study, we analyze hyperspectral image data and photos of hairless albino mice (C57BL/6) imaged at multiple time points after ultraviolet B (UVB) irradiation (*98*, *99*). As the primary environmental risk factor for nonmelanoma skin cancer, UVB irradiation is administered at a carcinogenic dose (2240 J m^{-2} three times per week for 10 weeks) to mimic the carcinogenic effects of sunlight (*100*, *101*). A pushbroom-type hyperspectral imaging system (*94*–*97*) provides reference measurements on the same mice immediately before or after smartphone photography (see note S4). The hyperspectral image data are analyzed using parametric spectral modeling of biological tissue to extract Hgb content on a pixel-by-pixel basis, serving as the ground truth (see Materials and Methods); Figure 5 (A and B) presents dorsal photos and the corresponding ground truth Hgb images of the same mouse at weeks 10 and 14 after the cessation of the carcinogenic dose of UVB irradiation (fig. S14, A and B).

We evaluate machine-readable Hgb quantification using a deep learning inflammation model that takes the recovered color values from a photo of mouse skin and outputs the corresponding tissue Hgb level (see note S4 and Fig. 5C) (*96*). In Fig. 5 (D and E) (fig. S14, C and D), Hgb images of the same mouse at weeks 10 and 14 are computed from photos acquired by Samsung Galaxy S21 and Apple iPhone 12 Pro, processed using neural network color recovery (HemaChrome) and adaptive regression color correction (Macbeth ColorChecker equivalent; fig. S6, A to C). Notably, the color correction using Macbeth ColorChecker overestimates Hgb content across both smartphone models, whereas the Hgb images recovered using

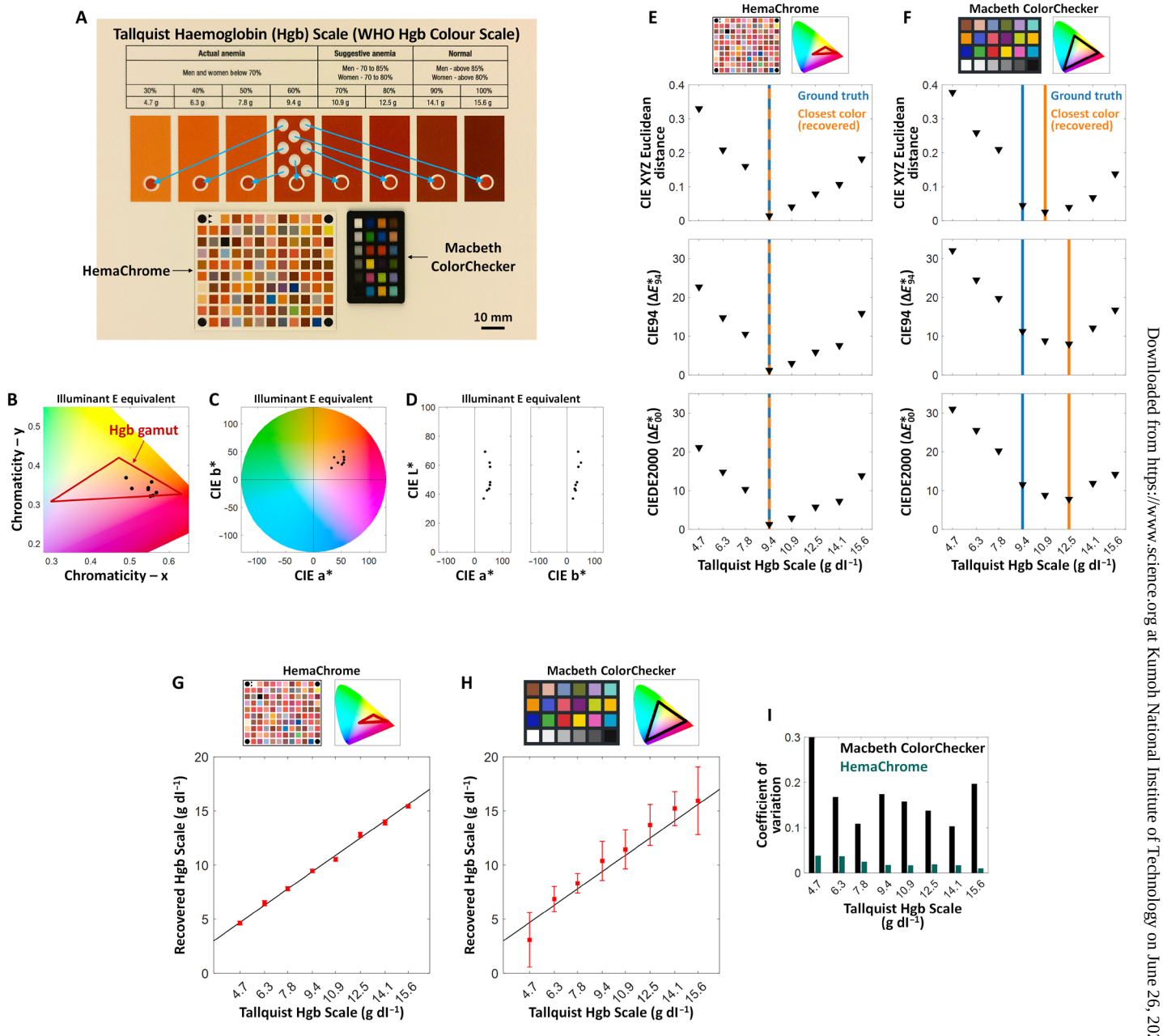

Fig. 4. Machine readability and quantification of blood Hgb colors with self-testing of Tallquist Haemoglobin Scale. (**A**) Representative photo of Tallquist Haemoglobin (Hgb) Scale (equivalent to WHO Haemoglobin Colour Scale) used as self-test samples, providing numerical readings of 4.7, 6.3, 7.8, 9.4, 10.9, 12.5, 14.1, and 15.6 g dl^{-1}. (**B**) CIE xy chromaticity values of Tallquist Hgb Scale under CIE illuminant E. (**C**) Corresponding CIE LAB values under CIE illuminant E on the *a** and *b** axes. (**D**) Corresponding L* values as functions of a* and b* values. (**E** and **F**) Color differences after color correction using HemaChrome (E) and Macbeth ColorChecker (F) for the Hgb scale patch of 9.4 g dl^{-1}. Three color metrics are calculated: CIE XYZ Euclidean distance, CIE94 (ΔE^*_{94}), and CIEDE2000 (ΔE^*_{00}). (**G**) Recovered Hgb levels using HemaChrome (neural network color recovery) and the actual Hgb levels (ground truth). Blood Hgb levels are directly computed from recovered color values under CIE illuminant E of Tallquist Hgb Scale, acquired under 36 various photo acquisition scenarios (Fig. 1G). Hgb levels are modeled as a univariate polynomial function of CIE X, Y, and Z values (see note S4). The scatter plot and the error bar represent the mean and the standard deviation (SD), respectively. The black line denotes the identity line. (**H**) Recovered Hgb levels using a Macbeth ColorChecker equivalent (adaptive regression color correction) and the actual Hgb levels. (**I**) Coefficients of variation for the blood Hgb levels recovered by HemaChrome and Macbeth ColorChecker from photos captured across 36 acquisition scenarios.

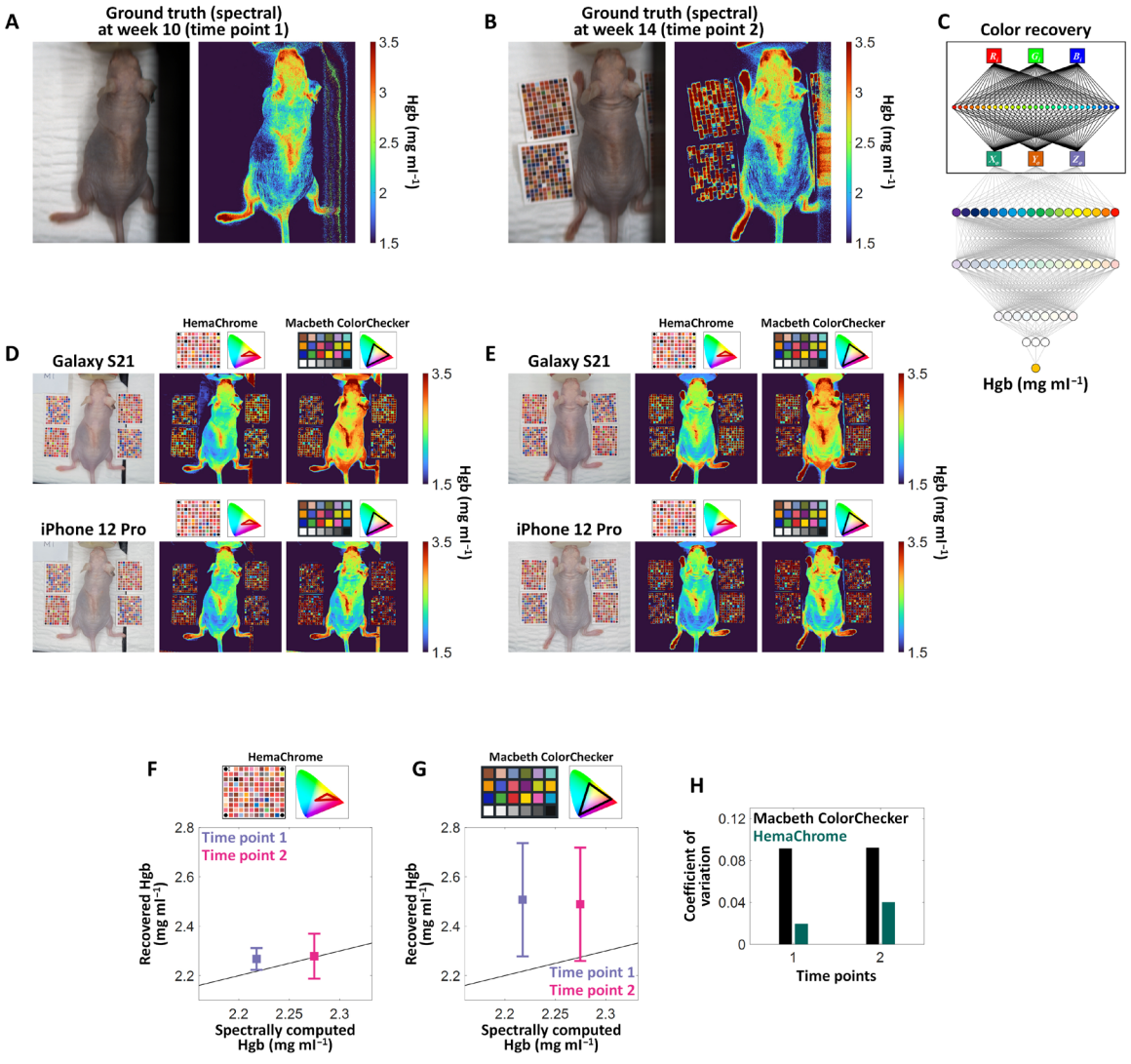

Fig. 5. Machine readability and learning of blood Hgb colors in inflammation bioimaging of experimental photocarcinogenesis. (**A** and **B**) Dorsal photos (left) and Hgb images (right) measured from conventional hyperspectral imaging (ground truth) of the same hairless albino mouse (C57BL/6) at weeks 10 (A) and 14 (B) after the cessation of a carcinogenic dose of ultraviolet B (UVB) irradiation. (**C**) Deep neural network model that estimates Hgb content using recovered color values under CIE illuminant E as input (see note S4). (**D** and **E**) Representative recovered Hgb images of the same mouse at weeks 10 (D) and 14 (E) from single-shot photos. Four distinct photo acquisitions, captured using Samsung Galaxy S21 and Apple iPhone 12 Pro and saved in RAW (i.e., DNG) and JPEG formats, are analyzed using HemaChrome (neural network color recovery) and a Macbeth ColorChecker equivalent (adaptive regression color correction). (**F**) Recovered Hgb values using HemaChrome and the spectrally computed Hgb values (ground truth). The recovered Hgb values are averaged over the entire dorsal area for each photo. The scatter plot and the error bar represent the mean and the SD, respectively. The black line denotes the identity line. (**G**) Recovered Hgb values using Macbeth ColorChecker and the spectrally computed Hgb values. (**H**) Coefficients of variation for the recovered Hgb values using HemaChrome and Macbeth ColorChecker from photos captured across four acquisition scenarios, calculated separately for each time point.

HemaChrome better match the spectrally measured Hgb images (ground truth). Figure 5 (F and G) (fig. S14, E and F) reveals the total Hgb values averaged over the entire dorsal area, as recovered from photos captured using the two smartphone models and two file formats (RAW and JPEG). The averaged Hgb values recovered using HemaChrome closely follow the spectrally computed Hgb values with small SDs at each time point (Fig. 5F, fig. S14E, and table S5). In contrast to HemaChrome, the conventional color correction (Macbeth ColorChecker) generates considerably larger variations of Hgb values (Fig. 5G, fig. S14F, and table S6). HemaChrome also exhibits lower coefficients of variation than Macbeth ColorChecker (Fig. 5H, fig. S14G, and eqs. S8 and S9).

Noninvasive mHealth blood Hgb assessment from peripheral tissue

We assess the machine color readability and learning of peripheral perfusion for an mHealth application designed for noninvasive blood Hgb assessment, compared with clinical laboratory testing. Blood Hgb testing is one of the most common clinical laboratory tests for various cases, including detecting anemia, blood disorders,

transfusion, hemorrhage, and acute kidney injury. Ongoing efforts focus on developing noninvasive point-of-care (POC) technologies using smartphones (*102*–*108*). The intrinsic challenge lies in ensuring accurate and precise color readings of the sensing site, unaffected by ambient light conditions or variations in smartphone/device models. We leverage a clinical study aimed at improving the quality of care for patients with sickle cell disease (SCD) by minimizing iatrogenic blood loss from frequent blood draws; blood Hgb levels are noninvasively estimated from photos of the palpebral conjunctiva (i.e., inner eyelid). The palpebral conjunctiva is an easily accessible peripheral tissue site that directly exposes surface microvasculature and lacks skin pigmentation (*96*, *105*, *108*–*110*), enabling reliable noninvasive blood Hgb assessment unaffected by skin color and tone variability.

Clinical data include photos of the palpebral conjunctiva captured immediately before or after clinical laboratory Hgb tests via venous blood draws, which serve as the gold standard, from 15 patients with SCD aged 14 to 73 years (Fig. 6A). This study focuses on reproducibility (inter-measurement reliability) by assessing the same patient with multiple smartphone photos acquired under diverse light conditions of sunlight, fluorescent tube, and white light-emitting diode (LED) in indoor settings (Fig. 6A). For inter-blood Hgb assessments, we use a substantial dataset of 156 photos from both the left and right eyelids in RAW (i.e., DNG) and JPEG formats captured with Samsung Galaxy S21 and Apple iPhone 12 Pro. For side-by-side comparisons, two sets of CIE XYZ values are recovered from the same photos (Fig. 6B) by separately applying neural network color recovery (HemaChrome) and adaptive regression color correction (Macbeth ColorChecker equivalent; fig. S6, A to C). The recovered color values of the palpebral conjunctiva under CIE illuminant E serve as the frontend input in the mHealth application (see note S4 and Fig. 6C).

Figure 6D presents the computed blood Hgb levels using HemaChrome across multiple photo acquisitions (table S7). The linear correlation between the recovered blood Hgb levels and clinical laboratory results shows a high correlation coefficient of 0.87 with narrow 95% limits of agreement (95% LOA) of (-2.51, 2.30 g dl^{-1}) and a bias of -0.11 g dl^{-1} in the Bland-Altman plot (Fig. 6D) (*111*). Notably, the range of the 95% LOA is highly comparable to that of capillary blood sampling (e.g., finger prick) tests (*47*, *106*). The pooled SD of the computed blood Hgb levels, capturing the reproducibility (table S7), returns a value of 1.26 g dl^{-1} (eq. S10). On the other hand, Fig. 6E shows the blood Hgb levels recovered using Macbeth ColorChecker across multiple photo acquisitions (table S8). The computed blood Hgb levels exhibit an underperforming correlation coefficient of 0.75, resulting in wide 95% LOA of (-3.88, 2.53 g dl^{-1}) and a bias of -0.67 g dl^{-1} in the Bland-Altman plot (Fig. 6E). The pooled SD of the computed blood Hgb levels (table S8) is higher at 6.26 g dl^{-1}. HemaChrome also reveals lower coefficients of variation compared to Macbeth ColorChecker across all patients (Fig. 6F and eqs. S8 and S9). Consequently, the color recovery using HemaChrome outperforms that of Macbeth ColorChecker for noninvasive blood Hgb assessments.

DISCUSSION

Device-, light-, and format-agnostic machine readability and learning of colors can open possibilities for digital health applications (*112*, *113*). First, remote POC diagnostics can be facilitated in at-home settings, where a telemedicine professional, interacting with the patient in their home environment, can remotely capture the patient's photos by taking screenshots on the health care professional's device. Traditionally, POC testing requires a health care professional to be physically close to the patient, whereas home tests are conducted by the patient or a guardian without professional oversight. The Food and Drug Administration has different regulatory pathways for POC and home tests (*114*). In this respect, machine readability and learning of colors may help bridge the regulatory gap between these two testing types. Second, commercially available off-the-shelf mobile devices, such as smartphones or laptops with onboard cameras, can be easily used without modifications or additional attachments, allowing patients to receive diagnostic services using their own devices. Third, existing picture archiving and communication systems (PACS) can be standardized and canonicalized to support multiple devices, image file formats, and clinical sites.

Machine readability and learning of colors in color-based diagnostic bioassays and bioimaging can further be enhanced using state-of-the-art three-color image sensors, advanced image file formats, and cutting-edge printing technologies. Advanced three-color image sensors can eliminate the need for demosaicing, which is a digital image processing technique used in conventional sensors (with a Bayer filter) to interpolate missing color information from neighboring pixels. For example, Foveon X3 sensors capture all three color values within the same pixel (*115*). Color routers can detect the entire color content without using a Bayer filter (*116*, *117*). An increase in color depth (or bit depth) in the R, G, and B channels can mitigate the possibility of metamerism, where different spectral profiles result in the same RGB values (*118*–*120*). File formats with higher color depth (e.g., RAW and High Efficiency Image File Format) can enable finer color distinctions, improving machine-readable color quantification. For example, a 10-bit color depth format consists of $2^{10\times3}$ combinations of RGB values (≈1.07 billion colors), while an 8-bit color depth format only generates $2^{8\times3}$ (≈16.77 million) colors. While pigment-based printing inks are constrained by their color fading, plasmonic structural paints can offer a promising solution for developing color reference charts with long-lasting durability and photostability (*121*).

In conclusion, the reported machine readability and learning platform of tissue colors can be applied to a wide range of color-based digital diagnostic applications. This platform leverages the reference color information physically present in samples to recover the absolute colors, regardless of photo acquisition settings. Reliably recovered color values of a sample of interest provide a foundation for advanced spectral analyses, including hyperspectral reconstruction (also known as spectral super-resolution, spectral reflectance estimation, spectral learning, or hypercolorization). The reported platform will also enhance color standardization and canonicalization, contributing to the evolving field of digital health alongside advances in computer color vision for biomedical imaging.

MATERIALS AND METHODS

Approximating CIE standard illuminant E using spectral normalization

Among CIE standard illuminants (also known as reference illuminants), CIE illuminant E stands out as a theoretical reference with a 100% uniform spectral power distribution across the entire wavelength range (equal energy radiator or spectrally uniform illumination) (*122*). Although CIE illuminant E is regarded as purely

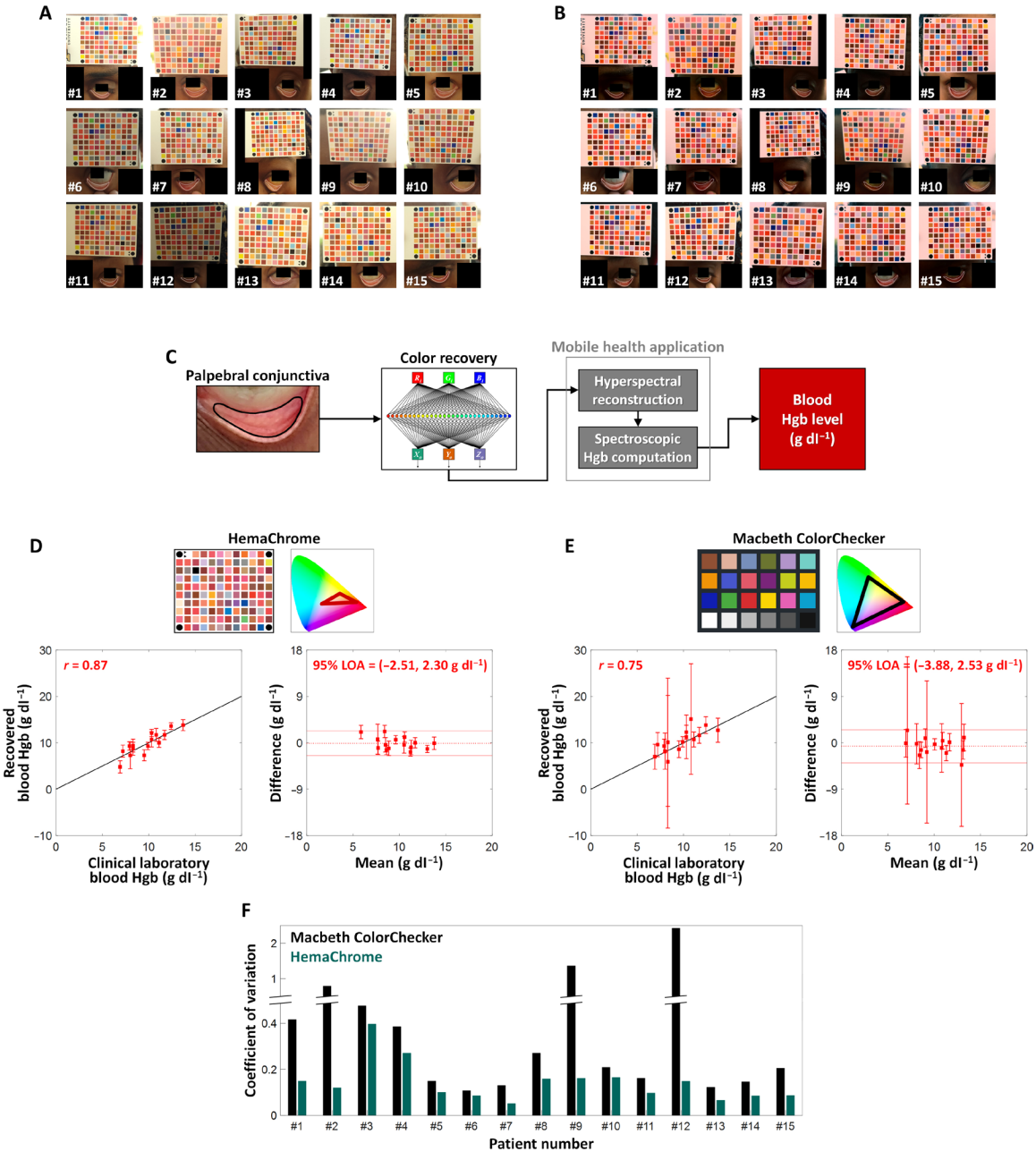

Fig. 6. Machine color readability and learning of peripheral tissue perfusion for noninvasive mHealth blood Hgb assessment. (**A**) Representative unprocessed smartphone photos of the palpebral conjunctiva (inner eyelid) juxtaposed with a HemaChrome chart captured under various light conditions. (**B**) CIE RGB images computed from recovered color values using HemaChrome (neural network color recovery). (**C**) mHealth application that estimates blood Hgb levels from single-shot photos using recovered color values under CIE illuminant E as input (see note S4). (**D**) Scatter plot between the recovered blood Hgb levels using HemaChrome and the clinical laboratory blood Hgb tests obtained from venous blood draws analyzed by a hematology analyzer (gold standard) and Bland-Altman analyses. For inter-blood Hgb assessments (reproducibility), 156 photos of both the left and right eyelids from 15 patients, acquired using Samsung Galaxy S21 and Apple iPhone 12 Pro and saved in RAW (i.e., DNG) and JPEG formats, are analyzed. The scatter plot and the error bar represent the mean and the SD, respectively. The black line denotes the identity line. (**E**) Scatter plot between the recovered blood Hgb levels using a Macbeth ColorChecker equivalent (adaptive regression color correction) and the clinical laboratory blood Hgb tests and Bland-Altman analyses. (**F**) Coefficients of variation for the recovered blood Hgb values computed for each patient using HemaChrome and Macbeth ColorChecker from photos captured across multiple photo acquisitions.

theoretical, spectral normalization using a reflectance standard effectively eliminates the spectral response of the illumination and system, making it equivalent to using CIE illuminant E. This approximation is made possible by the use of a white diffuse (Lambertian) reflectance standard having a reflectivity of >99% in the visible range. We obtained the spectral intensity $O(\lambda)$ reflected from a sample of interest under CIE illuminant E as follows: The spectral intensity $I_m(\lambda)$ reflected from the sample under an arbitrary light illumination, measured by a scientific laboratory spectrometer (VS140 VIS-NIR, Horiba Jobin Yvon, and SR-6VIS400-25, Ocean Optics), can be expressed as a function of the wavelength of light λ

$$I_m(\lambda) = L(\lambda) \cdot C(\lambda) \cdot D(\lambda) \cdot O(\lambda) \quad (1)$$

where $L(\lambda)$ is the spectral profile of the illumination light source, $C(\lambda)$ is the spectral response of all optical components in the system, and $D(\lambda)$ is the spectral response function (also known as spectral sensitivity) of the image sensor. Using a white diffuse reflectance standard (SRT-99-050, Labsphere), the spectral intensity $I_{ref}(\lambda)$ reflected from the white reflectance standard under the identical imaging setting as the sample can be obtained

$$I_{ref}(\lambda) = L(\lambda) \cdot C(\lambda) \cdot D(\lambda) \quad (2)$$

Then, $O(\lambda)$ is calculated by normalizing $I_m(\lambda)$ with respect to $I_{ref}(\lambda)$

$$O(\lambda) = \frac{I_m(\lambda)}{I_{ref}(\lambda)} \quad (3)$$

CIE illuminant E, through spectral normalization, allows for the definition of the absolute colors of a sample, as the spectral intensity is not influenced by the physical illumination source or acquisition conditions. This spectral normalization using a diffuse reflectance standard is commonly used in tissue optics and spectroscopy.

Gamut determination via parametric spectral modeling of biological tissue

To identify a physiologically relevant color gamut (Hgb gamut), we augmented physiologically relevant spectra of peripheral perfusion and blood microcirculation in the visible range (380 to 720 nm) by synthesizing data using parametric spectral modeling. The spectral intensity reflected from biological tissue can be expressed as a function of λ (*123*, *124*)

$$I(\lambda) = \left[\frac{\lambda}{\lambda_0}\right]^{a_1} \exp\left\{-a_2 \mu_a^{Total}(\lambda) \times \left[\frac{1-\exp\left[-a_3 \mu_a^{Total}(\lambda)\right]}{a_3 \mu_a^{Total}(\lambda)}\right]\right\} \quad (4)$$

where $\left[\lambda/\lambda_0\right]^{a_1}$ with $\lambda_0 = 500$ nm represents the tissue light scattering contribution, a_1 is the tissue (Rayleigh or Mie) scattering slope, a_2 is the blood volume fraction multiplied by the optical path length, and a_3 is the effective blood vessel diameter in tissue originating from the pigment packaging effect of red blood cells in microvessels, which is well-established in tissue optics (*123*, *125*). $\mu_a^{Total}(\lambda)$ is the total absorption coefficient including oxygenated and deoxygenated Hgb (*123*, *125*)

$$\mu_a^{Total}(\lambda) = a_4\left[a_5 \varepsilon_{HgbO_2}(\lambda) + (1-a_5)\varepsilon_{Hgb}(\lambda)\right] \quad (5)$$

where a_4 is the blood Hgb content, a_5 is the blood oxygen saturation, $\varepsilon_{HgbO_2}(\lambda)$ is the extinction coefficient of oxygenated Hgb, and $\varepsilon_{Hgb}(\lambda)$ is the extinction coefficient of deoxygenated Hgb.

First, we synthesized 12,240 spectral data of peripheral tissue in the visible range (Fig. 2E), using the physiologically relevant ranges of the model parameters (Table 1). We determined the ranges of parameters $a_1 \ldots a_5$ by analyzing spectral data from peripheral tissue in the existing clinical data (figs. S15 and S16). To solve the nonlinear optimization problem in Eqs. 4 and 5, the Nelder-Mead simplex method was used to obtain the model parameters (*126*)

$$\text{minimize } \|\boldsymbol{I}_m - \boldsymbol{I}\|_2^2 \quad (6)$$

where $\boldsymbol{I}_m = \left[I_m(\lambda_1), I_m(\lambda_2), \ldots, I_m(\lambda_N)\right]^T$ is the measured spectral intensity, and $\boldsymbol{I} = \left[I(\lambda_1), I(\lambda_2), \ldots, I(\lambda_N)\right]^T$ is the model-generated spectral intensity with $N = 341$ discrete wavelengths where λ ranges from 380 to 720 nm with a spectral interval of 1 nm. Then, we varied one parameter, while all other parameters were fixed at their average values in a step-by-step manner (Table 1). Second, we synthesized 10,000 spectral data of whole blood in the visible range (Fig. 2F) based on the physiological parameter ranges of blood Hgb levels $a_4 =$ 4 to 20 g dl^{-1} and blood oxygen saturation $a_5 =$ 50 to 100% (Table 1). To determine the color range of human blood Hgb samples, we modeled the spectral intensity based on the Beer-Lambert law using the total absorption coefficient of blood (Eq. 5)

$$I(\lambda) = \exp\left\{-a_4\left[a_5 \varepsilon_{HgbO_2}(\lambda) + (1-a_5)\varepsilon_{Hgb}(\lambda)\right] \times L\right\} \quad (7)$$

where L is the optical path length set to 0.1 mm, following the standard used by typical microcuvettes in commercial POC blood Hgb analyzers (e.g., HemoCue). Last, the Hgb gamut was defined using all of CIE XYZ and CIE LAB values derived from 10,000 spectral data of whole blood and 12,240 spectral data of peripheral tissue (see note S1).

Printing, reproducibility, and photostability (fade resistance)

To ensure the accessibility, practicality, and scalability of HemaChrome production, we used a commercially available inkjet printer (imagePROGRAF PRO-1000, Canon) equipped with 11 ink cartridges and a chroma optimizer (PFI-1000 LUCIA PRO Ink, Canon). We also implemented a printing calibration process to produce the desired colors for the color charts. The actual printed colors (output) exhibited variations from the intended colors (input), which were particularly influenced by the type of paper (print sheet) used. The CIE XYZ values of 116 reference colors designed for HemaChrome were used as input for printing (figs. S6, A to C, and S7). To ensure accurate color representation, the CIE XYZ values were converted to sRGB, and the final chart layout was completed in Adobe InDesign (Fig. 3B). For the printing calibration from input to output (printout), we applied the International Color Consortium (ICC) profile and used the manufacturer-recommended genuine paper (Photo Paper Premium Fine Art Smooth, Canon). After printing, we measured the reflectance spectra of all reference colors in the printed HemaChrome charts (fig. S5) using a spectrometer and a reflectance standard (equivalent to using CIE illuminant E). We confirmed that the resulting CIE xy chromaticity and CIE L* values (lightness) obtained from the measured spectra were within the Hgb gamut and the Hgb-related lightness range of 40 to 90 (Fig. 3, B to E). In addition, we assessed the printing reproducibility and the shelf-life of HemaChrome (see note S2).

Regression-based color corrections for conventional color charts

As the most commonly used color correction method using conventional color standards or reference charts (Macbeth ColorChecker or X-Rite ColorChecker), we applied regression-based color corrections (also known as lookup table and interpolation). For the simplest linear color correction, the mathematical relationship between the CIE XYZ under CIE illuminant E and the acquired RGB can be expressed (*53*, *56*, *60*, *62*, *63*)

$$\boldsymbol{y}_{3\times1} = \boldsymbol{T}_{3\times3}\boldsymbol{x}_{3\times1} \tag{8}$$

where $\boldsymbol{x}$ is a 3 × 1 vector corresponding to the three color values measured in the R, G, and B channels $\{\boldsymbol{x}_{3\times1} = [R, G, B]^{\mathrm{T}} = [I(R), I(G), I(B)]^{\mathrm{T}}\}$, $\boldsymbol{y}$ is a 3 × 1 vector of the CIE XYZ tristimulus values ($\boldsymbol{y}_{3\times1} = [X, Y, Z]^{\mathrm{T}}$), and $\boldsymbol{T}$ is a 3 × 3 matrix that converts the acquired RGB values to the corresponding CIE XYZ values under CIE illuminant E. In general, the number of reference colors (e.g., $k = 24$) in the conventional color charts was greater than the number of the unknowns (i.e., three color values). The incorporation of k different reference colors into Eq. 8 changes the underdetermined problem into an overdetermined problem

$$\boldsymbol{Y}_{3\times k} = \boldsymbol{T}_{3\times3}\boldsymbol{X}_{3\times k} \tag{9}$$

where $\boldsymbol{T}_{3\times3}$ can easily be solved using least-squares regression. We used fixed-design linear regression, including polynomial (or root-polynomial) expansion terms of R, G, and B values with appropriate powers (i.e., polynomial color correction) (*53*, *56*, *60*, *62*, *63*). Specifically, we included five typical types of higher-degree RGB polynomial or root-polynomial expansions. The acquired RGB vector $\boldsymbol{x}_{3\times1}$ was expanded to $\boldsymbol{x}^{j}_{p\times1}$, where $\boldsymbol{x}^{j}_{p\times1}$ denotes the j^{th} type of polynomial expansions with a total of p terms

Then, Eq. 9 can be rewritten

$$\boldsymbol{x}^{1}_{(p=4)\times1} = [1, R, G, B]^{\mathrm{T}},$$
$$\boldsymbol{x}^{2}_{(p=10)\times1} = \left[1, R, G, B, R^2, G^2, B^2, RG, GB, BR\right]^{\mathrm{T}},$$
$$\boldsymbol{x}^{3}_{(p=20)\times1} = \left[1, R, G, B, R^2, G^2, B^2, RG, GB, BR, R^3, G^3, B^3, R^2G, RG^2, G^2B, GB^2, B^2R, BR^2, RGB\right]^{\mathrm{T}},$$
$$\boldsymbol{x}^{4}_{(p=7)\times1} = \left[1, R, G, B, \sqrt{RG}, \sqrt{GB}, \sqrt{BR}\right]^{\mathrm{T}},$$
$$\boldsymbol{x}^{5}_{(p=14)\times1} = \left[1, R, G, B, \sqrt{RG}, \sqrt{GB}, \sqrt{BR}, \sqrt[3]{R^2G}, \sqrt[3]{RG^2}, \sqrt[3]{G^2B}, \sqrt[3]{GB^2}, \sqrt[3]{B^2R}, \sqrt[3]{BR^2}, \sqrt[3]{RGB}\right]^{\mathrm{T}} \tag{10}$$

$$\boldsymbol{Y}_{3\times k} = \boldsymbol{T}_{3\times p}\boldsymbol{X}^{j}_{p\times k} \tag{11}$$

Eq. 11 can be solved using the Moore-Penrose pseudoinverse

$$\boldsymbol{T}_{3\times p} = \boldsymbol{Y}_{3\times k}\left[\boldsymbol{X}^{j}_{p\times k}\right]^{+} \tag{12}$$

where + denotes the pseudoinverse. The matrix $\boldsymbol{T}_{3\times p}$ computed the CIE XYZ values under CIE illuminant E from the RGB values acquired in a specific acquisition setting. A suitable set of polynomial expansions (Eq. 10) must be manually selected for each photo acquisition, highly depending on devices, light conditions, and file formats (*53*, *56*, *60*, *62*, *63*).

Neural network–based color recovery for HemaChrome

We designed a fully connected neural network algorithm that accurately and precisely recovers CIE XYZ values under CIE illuminant E of a sample or scene in a fully automated manner. This neural network for color recovery is analogous to transduction learning (Fig. 3A) as opposed to inductive learning. For each photo, the known CIE XYZ under CIE illuminant E and acquired RGB values of the reference colors in HemaChrome served as the training dataset for the neural network. The weights of the connections between nodes across layers were specifically computed for a given scene or sample. Because of the small dataset size of 100 to 500 reference colors in HemaChrome (Fig. 3B and fig. S8, A and C), we intentionally used a concise neural network consisting of three layers: an input layer, a hidden layer, and an output layer (fig. S8B). The input layer had three nodes representing the RGB values acquired using a smartphone camera ($\boldsymbol{x}_{3\times1} = [R, G, B]^{\mathrm{T}}$), whereas the output layer with three nodes returned the recovered CIE XYZ values under CIE illuminant E ($\boldsymbol{y}_{3\times1} = [X, Y, Z]^{\mathrm{T}}$). A large number of 29 nodes in the hidden layer captured the nonlinearity between the recovered and acquired color values, which is conventionally modeled using different types of polynomial expansions in a manual manner (Eq. 10). The specifications of the neural network algorithm can be summarized as follows: For efficient training with a limited training dataset, the weights of network connections were initialized by sampling from a normal distribution with a mean of 0 and an SD of 0.01. Batch normalization was applied to the hidden layer. Sigmoid activation functions were used after batch normalization, as sigmoid functions outperform other activation functions in shallow neural networks, supported by the universal approximation theory (*81*, *82*). The neural network was trained using RMSEs over a maximum of 500 epochs. The Adam optimizer with an initial learning rate of 5×10^{-4} and a mini-batch size of 30 was used.

Ethics approval

The animal study was approved by the Institutional Animal Care and Use Committee at the Richard L. Roudebush Veterans' Administration Medical Center (protocol # VA 23028). The clinical human study was approved by the Institutional Review Board at Indiana University (protocol # 10056) and Purdue University (protocol # 2021-1225). Informed consent was obtained from all participants before enrollment.

Software for signal processing and statistical analyses

For data processing and algorithm developments, we analyzed the data using MATLAB (MATLAB R2021b, MathWorks) and PyTorch 2.0.1 in Python 3.9. For statistical analyses, we evaluated linear regression, correlations, t tests, and one-way analysis of variance (ANOVA), using STATA (STATA 18.0, StataCorp).

Supplementary Materials

The PDF file includes:

Supplementary Glossary Equations
Notes S1 to S4
Figs. S1 to S17
Tables S1 to S10
Legend for movie S1

Other Supplementary Material for this manuscript includes the following:

Movie S1

REFERENCES AND NOTES

1. E. P. Huang, J. P. B. O'Connor, L. M. McShane, M. L. Giger, P. Lambin, P. E. Kinahan, E. L. Siegel, L. K. Shankar, Criteria for the translation of radiomics into clinically useful tests. *Nat. Rev. Clin. Oncol.* **20**, 69–82 (2023).

2. E. J. Patterson, A. D. Bounds, S. K. Wagner, R. Kadri-Langford, R. Taylor, D. Daly, Oculomics: A crusade against the four horsemen of chronic disease. *Ophthalmol Therapy* **13**, 1427–1451 (2024).
3. R. K. Samala, K. Drukker, A. Shukla-Dave, H.-P. Chan, B. Sahiner, N. Petrick, H. Greenspan, U. Mahmood, R. M. Summers, G. Tourassi, T. M. Deserno, D. Regge, J. J. Näppi, H. Yoshida, Z. Huo, Q. Chen, D. Vergara, K. H. Cha, R. Mazurchuk, K. T. Grizzard, H. Huisman, L. Morra, K. Suzuki, S. G. Armato III, L. Hadjiiski, AI and machine learning in medical imaging: Key points from development to translation. *BJR. Artif. Intell.* **1**, ubae006 (2024).
4. A. Badano, C. Revie, A. Casertano, W.-C. Cheng, P. Green, T. Kimpe, E. Krupinski, C. Sisson, S. Skrøvseth, D. Treanor, P. Boynton, D. Clunie, M. J. Flynn, T. Heki, S. Hewitt, H. Homma, A. Masia, T. Matsui, B. Nagy, M. Nishibori, J. Penczek, T. Schopf, Y. Yagi, H. Yokoi, Summit on Color in Medical Imaging, Consistency and standardization of color in medical imaging: A consensus report. *J. Digit. Imaging* **28**, 41–52 (2015).
5. W.-C. Cheng, Color performance review (CPR): A color performance analyzer for endoscopy devices. *J. Imaging Sci. Technol.* **67**, 1–9 (2023).
6. S. R. Steinhubl, E. D. Muse, E. J. Topol, The emerging field of mobile health. *Sci. Transl. Med.* **7**, 283rv3 (2015).
7. C. S. Wood, M. R. Thomas, J. Budd, T. P. Mashamba-Thompson, K. Herbst, D. Pillay, R. W. Peeling, A. M. Johnson, R. A. McKendry, M. M. Stevens, Taking connected mobile-health diagnostics of infectious diseases to the field. *Nature* **566**, 467–474 (2019).
8. B. Hunt, A. J. Ruiz, B. W. Pogue, Smartphone-based imaging systems for medical applications: A critical review. *J. Biomed. Opt.* **26**, 040902 (2021).
9. T. Zoltie, S. Blome-Eberwein, S. Forbes, M. Theaker, W. Hussain, Medical photography using mobile devices. *BMJ* **378**, e067663 (2022).
10. G. D. Finlayson, Color in perspective. *IEEE Trans. Pattern Anal. Mach. Intell.* **18**, 1034–1038 (1996).
11. A. Gijsenij, T. Gevers, M. P. Lucassen, Perceptual analysis of distance measures for color constancy algorithms. *J. Opt. Soc. Am. A* **26**, 2243–2256 (2009).
12. D. H. Foster, Color constancy. *Vision Res.* **51**, 674–700 (2011).
13. R. Shamey, *Encyclopedia of Color Science and Technology* (Springer, 2023).
14. Y. Ohno, CIE fundamentals for color measurements. *NIP Digit. Fabri. Conf.* **16**, 540–545 (2000).
15. C. S. McCamy, H. Marcus, J. G. Davidson, A color-rendition chart. *J. Appl. Photogr. Eng.* **2**, 95–99 (1976).
16. M. E. Chevreul, *Des couleurs et de leurs applications aux arts industriels à l'aide des cercles chromatiques*. J. B. Baillière et fils, Paris, France. vol. Courtesy of Science History Institute. Rights: Public Domain Mark 1.0. https://doi.org/10.5479/sil.1077416.39088019378835.
17. D. Pascale, 2006. RGB Coordinates of the Macbeth Colorchecker. The BabelColor Company 6. https://babelcolor.com/index_htm_files/RGB Coordinates of the Macbeth ColorChecker.pdf.
18. Oxford, Bodleian Library MS. Savile 39; https://digital.bodleian.ox.ac.uk/objects/2c3ed6b8-6ae4-4c04-b45c-c1bbc0ac2ba0/.
19. U. Pinder, *Epiphanie Medicorum: Speculum videndi urinas hominum. Clauis aperiendi portas pulsuum. Berillus discernendi causas & differencias febrium* (Ulrich Pinder, 1506). https://books.google.co.kr/books?id=7iNfAAAAcAAJ.
20. Y. Yagi, Color standardization and optimization in whole slide imaging. *Diagn. Pathol.* **6**, 1–12 (2011).
21. X. Wang, D. Zhang, A new tongue colorchecker design by space representation for precise correction. *IEEE J. Biomed. Health Inform.* **17**, 381–391 (2013).
22. H. Wei, M. H. Brill, T. Park, Evaluation of targets for color calibrating digital images from an optical bright-field transmission microscope. *Color Res. Appl.* **40**, 577–584 (2015).
23. E. L. Clarke, C. Revie, D. Brettle, M. Shires, P. Jackson, R. Cochrane, R. Wilson, C. Mello-Thoms, D. Treanor, Development of a novel tissue-mimicking color calibration slide for digital microscopy. *Color Res. Appl.* **43**, 184–197 (2018).
24. B. Askarian, S.-C. Yoo, J. W. Chong, Novel image processing method for detecting strep throat (Streptococcal Pharyngitis) using smartphone. *Sensors* **19**, 3307 (2019).
25. M. Nixon, F. Outlaw, T. S. Leung, Accurate device-independent colorimetric measurements using smartphones. *PLOS ONE* **15**, e0230561 (2020).
26. T. Inoue, Y. Yagi, Color standardization and optimization in whole slide imaging. *Clin. Diagn. Pathol.* **4**, 10.15761/cdp.1000139 (2020).
27. M. Takahashi, R. Takahashi, Y. Morihara, I. Kin, K. Ogawa-Ochiai, N. Tsumura, Development of a camera-based remote diagnostic system focused on color reproduction using color charts. *Artif. Life Robot.* **25**, 370–376 (2020).
28. T. Kambara, Y. Ogino, A. Maeda, Y. Kajimura, "Development of color correction system for medical images using color charts," in *Proceedings SPIE 11709, Ultra-High-Definition Imaging Systems IV* (2021).
29. Y. Cai, "A novel imaging system for tongue inspection. IMTC/2002," in *Proceedings of the 19th IEEE Instrumentation and Measurement Technology Conference* (IEEE Cat. No.00CH37276) (2002), vol. 1, pp. 159–163.
30. R. D. Uthoff, B. Song, S. Sunny, S. Patrick, A. Suresh, T. Kolur, G. Keerthi, O. Spires, A. Anbarani, P. Wilder-Smith, M. A. Kuriakose, P. Birur, R. Liang, Point-of-care, smartphone-based, dual-modality, dual-view, oral cancer screening device with neural network classification for low-resource communities. *PLOS ONE* **13**, e0207493 (2018).
31. R. D. Uthoff, B. Song, S. Sunny, S. Patrick, A. Suresh, T. Kolur, K. Gurushanth, K. Wooten, V. Gupta, M. E. Platek, Small form factor, flexible, dual-modality handheld probe for smartphone-based, point-of-care oral and oropharyngeal cancer screening. *J. Biomed. Opt.* **24**, 106003 (2019).
32. J. Farrell, Z. Lyu, Z. Liu, H. Blasinski, Z. Xu, J. Rong, F. Xiao, B. Wandell, Soft-prototyping imaging systems for oral cancer screening. *Electron. Imaging* **32**, 212-1–212-7 (2020).
33. S. Van Poucke, Y. V. Haeghen, K. Vissers, T. Meert, P. Jorens, Automatic colorimetric calibration of human wounds. *BMC Med. Imaging* **10**, 7 (2010).
34. M. S. Kurecic, D. Antonic, I. Vranjkovic, "Custom colour reference target for chronic wound photography," in *AIC Colour Conference Proceedings* (2013), pp. 1353–1356.
35. B. T. Alayande, S. Prasad, M. Abimpaye, L. Bakorimana, A. Niyigena, J. Nkurunziza, V. K. Cubaka, F. Kateera, R. Fletcher, B. Hedt-Gauthier, Image-based surgical site infection algorithms to support home-based post-cesarean monitoring: Lessons from Rwanda. *PLoS Global Public Health* **3**, e0001584 (2023).
36. B. Zhang, B. V. Kumar, D. Zhang, Detecting diabetes mellitus and nonproliferative diabetic retinopathy using tongue color, texture, and geometry features. *IEEE Trans. Biomed. Eng.* **61**, 491–501 (2014).
37. B. Zhang, D. Zhang, Noninvasive diabetes mellitus detection using facial block color with a sparse representation classifier. *IEEE Trans. Biomed. Eng.* **61**, 1027–1033 (2014).
38. A. Raina, R. Hennessy, M. Rains, J. Allred, J. M. Hirshburg, D. Diven, M. K. Markey, Objective measurement of erythema in psoriasis using digital color photography with color calibration. *Skin Res. Technol.* **22**, 375–380 (2016).
39. D. August, Y. Kandasamy, R. Ray, K. New, D. Lindsay, Evaluation of the consistency of neonatal skin injury assessment using clinical images and the metric and graduated colour tool. *J. Tissue Viability* **31**, 395–403 (2022).
40. K. Noguchi, I. Saito, T. Namiki, Y. Yoshimura, T. Nakaguchi, Reliability of non-contact tongue diagnosis for Sjögrens syndrome using machine learning method. *Sci. Rep.* **13**, 1334 (2023).
41. A. Aune, G. Vartdal, G. Jimenez Diaz, L. M. Gierman, H. Bergseng, E. Darj, Iterative development, validation, and certification of a smartphone system to assess neonatal jaundice: Development and usability study. *JMIR Pediatr. Parent.* **6**, e40463 (2023).
42. Q. He, W. Li, Y. Shi, Y. Yu, W. Geng, Z. Sun, R. K. Wang, SpeCamX: Mobile app that turns unmodified smartphones into multispectral imagers. *Biomed. Opt. Express* **14**, 4929–4946 (2023).
43. L. Shen, J. A. Hagen, I. Papautsky, Point-of-care colorimetric detection with a smartphone. *Lab Chip* **12**, 4240–4243 (2012).
44. A. Y. Mutlu, V. Kılıç, G. K. Özdemir, A. Bayram, N. Horzum, M. E. Solmaz, Smartphone-based colorimetric detection via machine learning. *Analyst* **142**, 2434–2441 (2017).
45. M. Ra, M. S. Muhammad, C. Lim, S. Han, C. Jung, W.-Y. Kim, Smartphone-based point-of-care urinalysis under variable illumination. *IEEE J. Transl. Eng. Health Med.* **6**, 2800111 (2018).
46. M. E. Solmaz, A. Y. Mutlu, G. Alankus, V. Kılıç, A. Bayram, N. Horzum, Quantifying colorimetric tests using a smartphone app based on machine learning classifiers. *Sens. Actuators B* **255**, 1967–1973 (2018).
47. M. S. Perez-Plazola, E. A. Tyburski, L. R. Smart, T. A. Howard, A. Pfeiffer, R. E. Ware, W. A. Lam, P. T. McGann, AnemoCheck-LRS: An optimized, color-based point-of-care test to identify severe anemia in limited-resource settings. *BMC Med.* **18**, 337 (2020).
48. R. S. Weinstein, A. M. Lopez, B. A. Joseph, K. A. Erps, M. Holcomb, G. P. Barker, E. A. Krupinski, Telemedicine, telehealth, and mobile health applications that work: Opportunities and barriers. *Am. J. Med.* **127**, 183–187 (2014).
49. M. Takahashi, R. Koike, K. Nagasawa, Y. Manabe, H. Hirana, M. Takamura, T. Hongawa, I. Kimoto, K. Ogawa-Ochiai, N. Tsumura, Development of telemedicine tools with an emphasis on visual observation. *Artif. Life Robot.* **27**, 38–47 (2022).
50. D. Akkaynak, T. Treibitz, B. Xiao, U. A. Gürkan, J. J. Allen, U. Demirci, R. T. Hanlon, Use of commercial off-the-shelf digital cameras for scientific data acquisition and scene-specific color calibration. *J. Opt. Soc. Am. A* **31**, 312–321 (2014).
51. W.-C. Cheng, Reproducible color gamut of hematoxylin and eosin stained images in standard color spaces. *J. Pathol. Inform.* **11**, 36 (2020).
52. G. Simone, M. Gaiani, A. Bellabeni, A. Rizzi, Problems in image target-based color correction, in *Proceedings of IS&T International Symposium on Electronic Imaging: Color Imaging: Displaying, Processing, Hardcopy, and Applications* (2022), vol. **34**, pp. 141–142. https://doi.org/10.2352/EI.2022.34.15.COLOR-142.
53. V. Cheung, S. Westland, D. Connah, C. Ripamonti, A comparative study of the characterisation of colour cameras by means of neural networks and polynomial transforms. *Color. Technol.* **120**, 19–25 (2004).
54. A. Alsam, G. Finlayson, Integer programming for optimal reduction of calibration targets. *Color Res. Appl.* **33**, 212–220 (2008).
55. P. Menesatti, C. Angelini, F. Pallottino, F. Antonucci, J. Aguzzi, C. Costa, RGB color calibration for quantitative image analysis: The "3D Thin-Plate Spline" warping approach. *Sensors* **12**, 7063–7079 (2012).

56. G. D. Finlayson, M. Mackiewicz, A. Hurlbert, Color correction using root-polynomial regression. *IEEE Trans. Image Process.* **24**, 1460–1470 (2015).
57. S. Sunoj, C. Igathinathane, N. Saliendra, J. Hendrickson, D. Archer, Color calibration of digital images for agriculture and other applications. *ISPRS J. Photogramm. Remote Sens.* **146**, 221–234 (2018).
58. J. Marguier, N. Bhatti, H. Baker, M. Harville, S. Süsstrunk, Assessing human skin color from uncalibrated images. *Int. J. Imaging Syst. Technol.* **17**, 143–151 (2007).
59. R. Verma, J. Ali, A comparative study of various types of image noise and efficient noise removal techniques. *Int. J. Adv. Res. Comput. Sci. Softw. Eng.* **3**, (2013).
60. G. Simone, M. Gaiani, A. Ballabeni, A. Rizzi, Complex process of image color correction: A test of a target-based framework. *J. Opt. Soc. Am. A* **38**, 663–674 (2021).
61. I. Benito-Altamirano, D. Martínez-Carpena, O. Casals, C. Fábrega, A. Waag, J. D. Prades, Back-compatible color QR codes for colorimetric applications. *Pattern Recognit.* **133**, 108981 (2023).
62. P.-C. Hung, Colorimetric calibration in electronic imaging devices using a look-up-table model and interpolations. *J. Electron. Imaging* **2**, 53–61 (1993).
63. G. Hong, M. R. Luo, P. A. Rhodes, A study of digital camera colorimetric characterization based on polynomial modeling. *Color Res. Appl.* **26**, 76–84 (2001).
64. M. Delbracio, D. Kelly, M. S. Brown, P. Milanfar, Mobile computational photography: A tour. *Annu. Rev. Vis. Sci.* **7**, 571–604 (2021).
65. G. Finlayson, M. M. Darrodi, M. Mackiewicz, Rank-based camera spectral sensitivity estimation. *J. Opt. Soc. Am. A* **33**, 589–599 (2016).
66. Y. Ji, Y. Kwak, S. M. Park, Y. L. Kim, Compressive recovery of smartphone RGB spectral sensitivity functions. *Opt. Express* **29**, 11947–11961 (2021).
67. S. Tominaga, S. Nishi, R. Ohtera, Measurement and estimation of spectral sensitivity functions for mobile phone cameras. *Sensors* **21**, 4985 (2021).
68. G. Solomatov, D. Akkaynak, "Spectral sensitivity estimation without a camera," in *2023 IEEE International Conference on Computational Photography (ICCP)* (2023), pp. 1–12.
69. C. Li, M. R. Luo, M. Pointer, P. Green, Comparison of real colour gamuts using a new reflectance database. *Color Res. Appl.* **39**, 442–451 (2014).
70. M. Kato, H. Sato, Y. Mizokami, Effect of skin colors due to hemoglobin or melanin modulation on facial expression recognition. *Vision Res.* **196**, 108048 (2022).
71. Y. Lu, K. Xiao, C. Li, Facial redness perception based on realistic skin models. *London Imaging Meeting* **4**, 76–80 (2023).
72. V. R. Weir, K. Dempsey, J. W. Gichoya, V. Rotemberg, A.-K. I. Wong, A survey of skin tone assessment in prospective research. *NPJ Digit. Med.* **7**, 191 (2024).
73. T. Smith, J. Guild, The CIE colorimetric standards and their use. *Trans. Opt. Soc.* **33**, 73 (1931).
74. E. Reinhard, E. A. Khan, A. O. Akyuz, G. Johnson, *Color Imaging: Fundamentals and Applications* (CRC Press, 2008).
75. C. Poynton, *Digital Video and HD: Algorithms and Interfaces* (Elsevier, 2012).
76. CIE publication 116: Industrial colour-difference evaluation (CIE Central Bureau, 1995).
77. R. McDonald, K. J. Smith, CIE94-A new colour-difference formula. *J. Soc. Dyers Colour* **111**, 376–379 (1995).
78. M. R. Luo, G. Cui, B. Rigg, The development of the CIE 2000 colour-difference formula: CIEDE2000. *Color Res. Appl.* **26**, 340–350 (2001).
79. G. Sharma, W. Wu, E. N. Dalal, The CIEDE2000 color-difference formula: Implementation notes, supplementary test data, and mathematical observations. *Color Res. Appl.* **30**, 21–30 (2005).
80. P. Schneider, F. Xhafa, *Anomaly Detection and Complex Event Processing over IoT Data Streams: With Application to eHealth and Patient Data Monitoring* (Academic Press, 2022).
81. G. Cybenko, Approximation by superpositions of a sigmoidal function. *Math. Control. Signals Syst.* **2**, 303–314 (1989).
82. K. Hornik, Approximation capabilities of multilayer feedforward networks. *Neural Netw.* **4**, 251–257 (1991).
83. L. Von Rueden, S. Mayer, K. Beckh, B. Georgiev, S. Giesselbach, R. Heese, B. Kirsch, J. Pfrommer, A. Pick, R. Ramamurthy, Informed machine learning–A taxonomy and survey of integrating prior knowledge into learning systems. *IEEE Trans. Knowl. Data Eng.* **35**, 614–633 (2021).
84. G. E. Karniadakis, I. G. Kevrekidis, L. Lu, P. Perdikaris, S. Wang, L. Yang, Physics-informed machine learning. *Nat. Rev. Phys.* **3**, 422–440 (2021).
85. A. Kadambi, C. de Melo, C.-J. Hsieh, M. Srivastava, S. Soatto, Incorporating physics into data-driven computer vision. *Nat. Mach. Intell.* **5**, 572–580 (2023).
86. J. Critchley, I. Bates, Haemoglobin colour scale for anaemia diagnosis where there is no laboratory: A systematic review. *Int. J. Epidemiol.* **34**, 1425–1434 (2005).
87. H. Marn, J. A. Critchley, Accuracy of the WHO haemoglobin colour scale for the diagnosis of anaemia in primary health care settings in low-income countries: A systematic review and meta-analysis. *Lancet Glob. Health* **4**, e251–e265 (2016).
88. Y.-I. Kwon, A review of the characteristics of early apparatus and methods for hemoglobin estimation. *Korean J. Clin. Lab. Sci.* **48**, 401–410 (2016).
89. R. L. Konger, Z. Xu, R. P. Sahu, B. M. Rashid, S. R. Mehta, D. R. Mohamed, S. C. DaSilva-Arnold, J. R. Bradish, S. J. Warren, Y. L. Kim, Spatiotemporal assessments of dermal hyperemia enable accurate prediction of experimental cutaneous carcinogenesis as well as chemopreventive activity. *Cancer Res.* **73**, 150–159 (2013).
90. C. Nishigori, Photocarcinogenesis and Inflammation. *Cancer and Inflammation Mechanisms: Chemical, Biological, and Clinical Aspects* (2014), pp. 271–283.
91. S. Subhadarshani, M. Athar, C. A. Elmets, Photocarcinogenesis. *Curr. Dermatol. Rep.* **9**, 189–199 (2020).
92. R. L. Konger, L. Ren, R. P. Sahu, E. Derr-Yellin, Y. L. Kim, Evidence for a non-stochastic two-field hypothesis for persistent skin cancer risk. *Sci. Rep.* **10**, 19200 (2020).
93. A. L. Shugar, R. L. Konger, C. A. Rohan, J. B. Travers, Y. L. Kim, Mapping cutaneous field carcinogenesis of nonmelanoma skin cancer using mesoscopic imaging of pro-inflammation cues. *Exp. Dermatol.* **33**, e15076 (2024).
94. G. Lu, B. Fei, Medical hyperspectral imaging: A review. *J. Biomed. Opt.* **19**, 010901 (2014).
95. M. Torabzadeh, P. Stockton, G. T. Kennedy, R. B. Saager, A. J. Durkin, R. A. Bartels, B. J. Tromberg, Hyperspectral imaging in the spatial frequency domain with a supercontinuum source. *J. Biomed. Opt.* **24**, 071614 (2019).
96. Y. Ji, S. M. Park, S. Kwon, J. W. Leem, V. V. Nair, Y. Tong, Y. L. Kim, mHealth hyperspectral learning for instantaneous spatiospectral imaging of hemodynamics. *PNAS Nexus* **2**, pgad111 (2023).
97. M. H. Tran, B. Fei, Compact and ultracompact spectral imagers: Technology and applications in biomedical imaging. *J. Biomed. Opt.* **28**, 040901 (2023).
98. R. L. Konger, E. Derr-Yellin, D. Hojati, C. Lutz, J. P. Sundberg, Comparison of the acute ultraviolet photoresponse in congenic albino hairless C57BL/6J mice relative to outbred SKH1 hairless mice. *Exp. Dermatol.* **25**, 688–693 (2016).
99. A. Y. Voigt, M. Michaud, K. Y. Tsai, J. Oh, J. P. Sundberg, Differential hairless mouse strain-specific susceptibility to skin cancer and sunburn. *J. Invest. Dermatol.* **139**, 1837–1840.e3 (2019).
100. A. P. Pentland, J. W. Schoggins, G. A. Scott, K. N. M. Khan, R. Han, Reduction of UV-induced skin tumors in hairless mice by selective COX-2 inhibition. *Carcinogenesis* **20**, 1939–1944 (1999).
101. T. A. Wilgus, A. T. Koki, B. S. Zweifel, D. F. Kusewitt, P. A. Rubal, T. M. Oberyszyn, Inhibition of cutaneous ultraviolet light B–mediated inflammation and tumor formation with topical celecoxib treatment. *Mol. Carcinog.* **38**, 49–58 (2003).
102. J. McMurdy, G. Jay, S. Suner, G. Crawford, Photonics-based in vivo total hemoglobin monitoring and clinical relevance. *J. Biophotonics* **2**, 277–287 (2009).
103. E. J. Wang, W. Li, J. Zhu, R. Rana, S. N. Patel, Noninvasive hemoglobin measurement using unmodified smartphone camera and white flash. *Annu. Int. Conf. IEEE Eng. Med. Biol. Soc.* 2017, 2333–2336 (2017).
104. R. G. Mannino, D. R. Myers, E. A. Tyburski, C. Caruso, J. Boudreaux, T. Leong, G. Clifford, W. A. Lam, Smartphone app for non-invasive detection of anemia using only patient-sourced photos. *Nat. Commun.* **9**, 4924 (2018).
105. S. M. Park, M. A. Visbal-Onufrak, M. M. Haque, M. C. Were, V. Naanyu, M. K. Hasan, Y. L. Kim, mHealth spectroscopy of blood hemoglobin with spectral super-resolution. *Optica* **7**, 563–573 (2020).
106. R. An, Y. Huang, Y. Man, R. W. Valentine, E. Kucukal, U. Goreke, Z. Sekyonda, C. Piccone, A. Owusu-Ansah, S. Ahuja, J. A. Little, U. A. Gurkan, Emerging point-of-care technologies for anemia detection. *Lab Chip* **21**, 1843–1865 (2021).
107. M. K. Hasan, M. H. Aziz, M. I. I. Zarif, M. Hasan, M. Hashem, S. Guha, R. R. Love, S. Ahamed, Noninvasive hemoglobin level prediction in a mobile phone environment: State of the art review and recommendations. *JMIR mHealth uHealth* **9**, e16806 (2021).
108. S. M. Park, Y. Ji, S. Kwon, J. W. Leem, A. R. W. O'Brien, Y. Wang, Y. L. Kim, Remote blood hemoglobin monitoring with hyperspectral color truthing for advancing sickle cell care. *Blood* **142**, 2277 (2023).
109. G. Dimauro, M. E. Griseta, M. G. Camporeale, F. Clemente, A. Guarini, R. Maglietta, An Intelligent non-invasive system for automated diagnosis of anemia exploiting a novel dataset. *Artif. Intell. Med.* **136**, 102477 (2023).
110. L. Zhao, A. Vidwans, C. J. Bearnot, J. Rayner, T. Lin, J. Baird, S. Suner, G. D. Jay, Prediction of anemia in real-time using a smartphone camera processing conjunctival images. *PLOS ONE* **19**, e0302883 (2024).
111. D. Giavarina, Understanding bland altman analysis. *Biochem. Med.* **25**, 141–151 (2015).
112. S. A. Boppart, R. Richards-Kortum, Point-of-care and point-of-procedure optical imaging technologies for primary care and global health. *Sci. Transl. Med.* **6**, 253rv2 (2014).
113. E. M. Euliano, A. A. Sklavounos, A. R. Wheeler, K. J. McHugh, Translating diagnostics and drug delivery technologies to low-resource settings. *Sci. Transl. Med.* **14**, eabm1732 (2022).
114. C. M. Kepczynski, J. A. Genigeski, R. R. Koski, A. C. Bernknopf, A. M. Konieczny, M. E. Klepser, A systematic review comparing at-home diagnostic tests for SARS-CoV-2: Key points for pharmacy practice, including regulatory information. *J. Am. Pharm. Assoc.* **61**, 666–677.e2 (2021).
115. J. Zhang, "Film-like images with super-fine details using foveon X3 technology," in *Imaging and Applied Optics 2017 (3D, AIO, COSI, IS, MATH, pcAOP)* OSA Technical Digest (Optica Publishing Group, 2017), paper. IM3E.4.

116. N. Zhao, P. B. Catrysse, S. Fan, Perfect RGB-IR color routers for sub-wavelength size CMOS image sensor pixels. *Adv. Photon. Res.* **2**, 2000048 (2021).
117. X. Zou, Y. Zhang, R. Lin, G. Gong, S. Wang, S. Zhu, Z. Wang, Pixel-level bayer-type colour router based on metasurfaces. *Nat. Commun.* **13**, 3288 (2022).
118. D. H. Foster, K. Amano, S. M. Nascimento, M. J. Foster, Frequency of metamerism in natural scenes. *J. Opt. Soc. Am. A* **23**, 2359–2372 (2006).
119. W. J. Cukierski, D. J. Foran, Metamerism in multispectral imaging of histopathology specimens. *Proc. IEEE Int. Symp. Biomed. Imaging* **2010**, 145–148 (2010).
120. K. Jacob, Medical Photography: Limitless Applications (2016); https://appliedclinicaltrialsonline.com/view/medical-photography-limitless-applications.
121. P. Cencillo-Abad, D. Franklin, P. Mastranzo-Ortega, D. Chanda, Ultralight plasmonic structural color paint. *Sci. Adv.* **9**, eadf7207 (2023).
122. J. Schanda, *Colorimetry: Understanding the CIE System* (John Wiley & Sons, 2007).
123. J. C. Finlay, T. H. Foster, Effect of pigment packaging on diffuse reflectance spectroscopy of samples containing red blood cells. *Opt. Lett.* **29**, 965–967 (2004).
124. A. Amelink, D. J. Robinson, H. J. Sterenborg, Confidence intervals on fit parameters derived from optical reflectance spectroscopy measurements. *J. Biomed. Opt.* **13**, 054044 (2008).
125. N. Rajaram, A. Gopal, X. Zhang, J. W. Tunnell, Experimental validation of the effects of microvasculature pigment packaging on in vivo diffuse reflectance spectroscopy. *Lasers Surg. Med.* **42**, 680–688 (2010).
126. J. C. Lagarias, J. A. Reeds, M. H. Wright, P. E. Wright, Convergence properties of the nelder–mead simplex method in low dimensions. *SIAM J. Optim.* **9**, 112–147 (1998).

Acknowledgments: We thank A. Pucka, B. A. Reyes, T. J. Barrett, and N. Dutt for the clinical data collection from sickle cell patients at the Indiana University School of Medicine. In addition, we thank E. Derr-Yellin for the animal study and imaging at the Indiana University School of Medicine and the Richard L. Roudebush Veterans' Administration Medical Center. We also thank M. Keller, W. Wang, S. Kulhare, and D. Banik from Global Health Labs for valuable discussion. **Funding:** This work was supported by the National Institutes of Health grant R01EB033788 (Y.L.K.), Department of Veterans Affairs grant I01BX005816 (R.L.K. and Y.L.K.), National Institutes of Health grant R21TW012486 (Y.L.K.), National Institutes of Health grant R33TW012486 (Y.L.K.), National Institutes of Health grant R01AG048946 (Y.L.K.), National Institutes of Health Technology Accelerator Challenge Prize (Y.L.K.), Global Health Labs/Gates Ventures (Y.L.K.), and Engineering in Medicine Pilot Project supported by Purdue University College of Engineering and Indiana University School of Medicine (Y.W. and Y.L.K.). **Author contributions:** Conceptualization: S.M.P., S.K., Y.J., and Y.L.K. Methodology: S.M.P., S.K., Y.J., R.L.K., and Y.L.K. Software: S.M.P., S.K., Y.J., H.S., J.H., and Y.L.K. Validation: S.M.P., S.K., Y.J., H.S., J.W.L., Y.W., and Y.L.K. Formal analysis: S.M.P., S.K., Y.J., J.W.L., Y.K., J.H., and Y.L.K. Investigation: S.M.P., S.K., Y.J., J.W.L., Y.K., R.L.K., Y.W., and Y.L.K. Resources: S.M.P., S.K., Y.J., G.T.-C.C., A.R.O., R.L.K., Y.W., and Y.L.K. Data curation: S.M.P., S.K., Y.J., J.W.L., Y.K., Y.W., and Y.L.K. Writing—original draft: S.M.P., Y.J., and Y.L.K. Writing—review and editing: S.M.P., Y.J., J.H., A.R.O., R.L.K., and Y.L.K. Visualization: S.M.P., Y.J., and Y.L.K. Supervision: S.M.P., Y.J., G.T.-C.C., A.R.O., R.L.K., Y.W., and Y.L.K. Project administration: S.M.P., Y.J., Y.W., and Y.L.K. Funding acquisition: Y.W., R.L.K., and Y.L.K. **Competing interests:** Y.L.K. is a founding member of HemaChrome LLC. S.M.P., S.K., Y.J., J.W.L., and Y.L.K. filed patent applications (PCT/US24/25608 and PCT/US24/25609) via Purdue Research Foundation on 20 April 2024. The remaining authors declare that they have no competing interests. **Data and materials availability:** All data needed to evaluate the conclusions in the paper are present in the paper and/or the Supplementary Materials. Patient data, which could compromise participant privacy and consent, have been deidentified and presented in the main text and/or the Supplementary Materials. The computational models and algorithms used in this study rely on standard toolboxes and libraries that are publicly available in MATLAB and PyTorch.

Submitted 27 September 2024
Accepted 29 April 2025
Published 4 June 2025
10.1126/sciadv.adt4831